Department of AERONAUTICS and ASTRONAUTICS
STANFORD UNIVERSITY

Final Report

for the Period

August 1, 1994 to September 30, 1996

on

PARTICLE/CONTINUUM HYBRID SIMULATION IN A PARALLEL COMPUTING ENVIRONMENT

Grant No. NCC2-5072

Submitted to

NASA-Ames Research Center
Moffett Field, California 94035-1000
W.J. Feiereisen - Technical Officer

by the

Department of Aeronautics and Astronautics
Stanford University, Stanford, California 94305

Donald Baganoff - Principal Investigator

November 1, 1996

I. INTRODUCTION

This final report is for work carried out under Grant No. NCC2-5072 during the period from August 1, 1994 to September 30, 1996.

The objective of this study was to modify an existing parallel particle code, based on the direct simulation Monte Carlo (DSMC) method, to include a Navier-Stokes (NS) calculation so that a hybrid solution could be developed. The former was developed by McDonald, Fallavollita and Dahlby at Stanford University for use on the Intel Gamma, Delta, and Paragon computers. The need for a hybrid DSMC/NS solution arises, for example, in situations in which a cold blunt body is placed in a high enthalpy flow. The very high stagnation temperature and pressure produced, together with the cold body, cause the gas density near the surface to become quite high; the density ratio across the thermal layer can be 30 or greater. Because of the high density and the large gradients present, use of the DSMC method alone becomes computationally costly. The aim was to make use of a Navier-Stokes code to handle all near-continuum sub-regions, such as the thermal layer or a boundary layer in general.

In carrying out the work, it was determined that the following five issues had to be addressed before extensive program development for 3D capability was pursued:

(*i*) find a set of one-sided kinetic fluxes that are fully compatible with the DSMC method, so that they may be used in interfacing the two solution schemes;

(*ii*) develop a finite volume scheme that makes use of these one-sided kinetic fluxes;

(*iii*) make use of the one-sided kinetic fluxes together with DSMC type boundary conditions at a material surface so that velocity slip and temperature slip arise naturally for near-continuum conditions;

(*iv*) find a suitable sampling scheme so that the values of the one-sided fluxes predicted by the NS solution at an interface between the two domains can be converted into the correct distribution of particles to be introduced into the DSMC domain; and

(*v*) carry out a suitable number of tests to confirm that the developed concepts are valid, individually and in concert for a hybrid scheme.

The first three issues were addressed by S. Chou and elegantly handled in his Ph.D. thesis [1], and in a follow-on paper which was recently accepted for publication in the Journal for Computational Physics [2]. It became possible to address the fourth issue directly by making use of the analytic expressions developed by Chou, and its implementation is discussed in the two theses by D. Dahlby [3] and by T. Lou [4]. The fifth issue was studied by Lou [4] and by Lou et al. [5] for one-dimensional geometries, and by Dahlby [3] and Duttweiler [7] for two dimensional geometries. Presentations of the work were made by Dahlby [6] and most recently by Duttweiler [7]. All of the listed work was supported, to varying degrees, by the grant.

Because much of the work has been reported in student theses and represents many pages of text, only a short review of the relevant topics, which can be used as a guide to the publications themselves, will be given. On the other hand, the two papers [2] and [5] have yet to appear as archive journal publications and so copies are attached as Appendices A and B.

II. Split Kinetic Fluxes, Numerical Studies

Starting with the kinetic-theory definition for the split kinetic fluxes, their derivation and development for the Chapman-Enskog velocity distribution function were carried out by Chou [1], and a listing of the resultant set of relations for the split fluxes is given as Eqs. (38)-(44) in Appendix A. The appropriate boundary conditions for the split fluxes are described by Eqs. (62)-(68) in the same appendix. These boundary conditions are flux-type boundary conditions and therefore lead to both temperature slip and velocity slip at a material surface. A version of the monotone upstream-centered scheme for conservation laws (MUSCL) was used in applying the split kinetic flux relations to obtain numerical solutions for the NS equations for various test flows, as described on page 11 of Appendix A. Numerical tests on the split kinetic fluxes were carried out for the highly viscous and heat conducting flow found in a normal shock wave profile (App. A, Figs. 5 and 6) and for the opposite limit represented by the Euler flow in the shock tube problem (Figs. 7 and 8). As shown in the figures, comparisons were made with numerical solutions to the Navier-Stokes equations based on the established methods of Roe and Jameson (SLIP2). Additionally, tests involving a solid surface were used to study the thermal boundary layer

found near an impulsively started piston (App. A, Figs. 1 and 9), which leads to temperature slip, along with tests involving the viscous, heat conducting flow found in the slider-plate or lid-driven cavity problem (Figs. 10 - 12), which introduces both temperature and velocity slip. As seen in the figures, all comparisons are uniformly good.

III. Confirmation of Split Kinetic Fluxes and Slip

Because the split kinetic fluxes are derived for the nonequilibrium state represented by the Chapman-Enskog velocity distribution function, it is expected that the values predicted by the analytic expressions should agree with results of simulations using the direct simulation Monte Carlo (DSMC) method, as long as the Knudsen number, velocity gradients, and temperature gradients are suitably small in the simulated flow. In addition, because the boundary conditions used in the two methods are physically identical, one would expect good agreement for all slip values as well. Studies of this hypothesis were carried out by Dahlby [3] and by Lou [4], and a paper summarizing the work [5] is reproduced as Appendix B. The tests were conducted for conditions of flow (Knudsen number and dimensionless time) in which both methods (DSMC and NS) alone were capable of providing the physically correct prediction, and thus should agree. Three test cases were studied.

The first case considered an impulsively started piston in a stationary equilibrium gas, and confirmation that the temperature and density profiles in the thermal layer agree after roughly 10 collision times is shown in Figs. 2 and 3 in Appendix B. Because the numerical value of temperature slip for this case is small and on the order of 10%, and because sampling in the DSMC method is severely limited in a nonsteady problem where time averaging in not permitted, accurate DSMC values are difficult to obtain. Still, the comparison shown in Fig. 4 of Appendix B is remarkably good. The split fluxes for mass, momentum and energy were recorded at the wall in the DSMC method by monitoring the particles that cross from the gas into the wall region during a time step. Comparisons between theory and simulation are presented in Figs. 5 and 6, showing outstanding agreement for the split fluxes.

The second test considered an impulsively started flat plate moving parallel to its surface in a stationary equilibrium gas. Here the nonequilibrium is caused by the

velocity field and to a lesser degree by the temperature field. The velocity slip at the plate surface is displayed in Fig. 8 of Appendix B for the two methods showing remarkably good agreement. Likewise, the split fluxes are given in Figs. 9 and 10 offering equally good agreement.

The third test considered the steady state solution for the slider plate problem, where a two-dimensional square cavity filled with a gas is closed by a moving plate. The most impressive comparisons are given by the tangential velocity, Fig. 13, and the split fluxes, Fig. 14, at the surface of the cavity. Together, these three tests verify that the analytic expressions we are using for the split kinetic fluxes are in full agreement with results of simulations using the direct simulation Monte Carlo method.

IV. Sampling from the Chapman-Enskog Distribution

To implement a DSMC/NS hybrid scheme based on the passing of split-fluxes, one must be able to use the data from the NS solution (at the interface and at each time step) to create a proper sample of particles for insertion into the DSMC region. This collection of particles must carry the correct mass, momentum, and energy and in order to do so must represent a sample from a weighted Chapman-Enskog velocity distribution. A straightforward selection/rejection scheme is far too computationally costly, for a complex 3D function such as the CE distribution, and a less expensive method must be found. Conceptually, a superior procedure can be understood by a review of Fig. 1, where the equivalent 2D problem is considered. Taking Cx and Cy to be the two components of molecular velocity and assuming we are interested in the positive directed flux along the x-axis, then one need only consider the portion of the velocity distribution function shown in the first row. However, if we are interested in the distribution that makes up the one-way flux, then we need the product of Cx and $f(Cx, Cy)$ which is the weighted distribution shown in the second row. If this distribution is integrated over the entire Cx domain, one then obtains a probability density that is a function of Cy alone, namely the marginal distribution, as shown in the dashed plane of the mesh plot of the third row. On creating the indefinite integral of this function, as displayed in the right-hand column, one obtains the probability that the y-component of the molecular velocity is smaller than some Cy for all values of Cx. This function can then be used to randomly pick a value of Cy

for a sample particle by first selecting a random number $0 \leq R1 \leq 1$ and then finding the corresponding value of Cy from the plot. This value for Cy is then used in the distribution shown in the second row to obtain a function of Cx alone, as depicted by the dashed plane in the mesh plot of the fourth row.

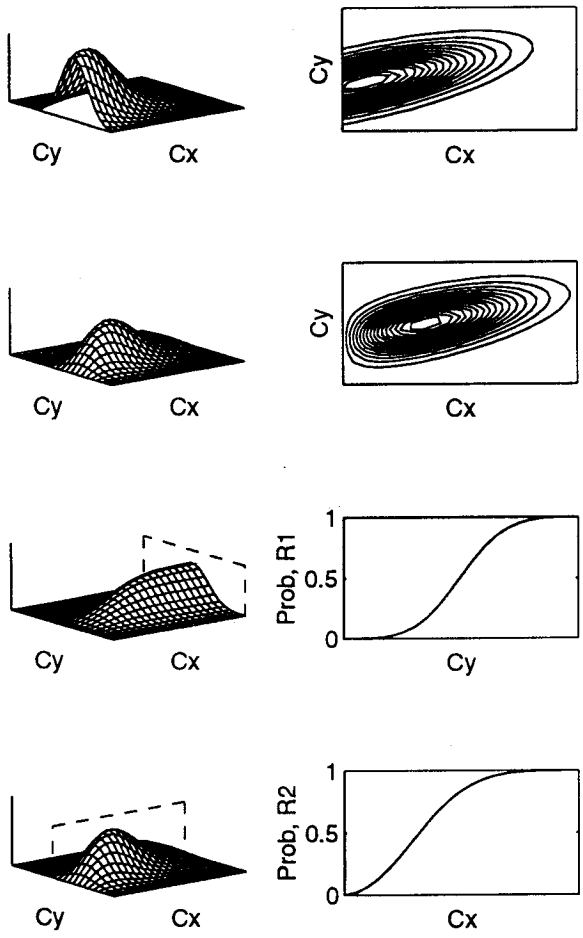

Fig. 1. Procedure for selecting a pair of random velocities Cx and Cy, from the weighted Chapman-Enskog distribution.

On creating the indefinite integral of this function, as displayed in the right-hand column, one obtains the probability that the x-component of the molecular velocity is smaller than some Cx for the particular value of Cy selected. This function can then be used to randomly pick a value of Cx for the sample particle, by first selecting a random number $0 \leq R2 \leq 1$ and then finding the corresponding value of Cx from

the plot. In summary, we pick two random numbers $R1$ and $R2$ to select two random velocities Cx and Cy for our first sample particle; and these steps are then repeated for all particles to be sampled.

A typical sample for 200 particles is shown in Fig. 2, superposed on a contour plot of the weighted distribution itself, verifying the effectiveness of the procedure. We are able to use this procedure because all of the analytic expressions for the integrals needed, both definite and indefinite, were previously obtained by Chou in the process of developing his analytic results for the split kinetic fluxes.

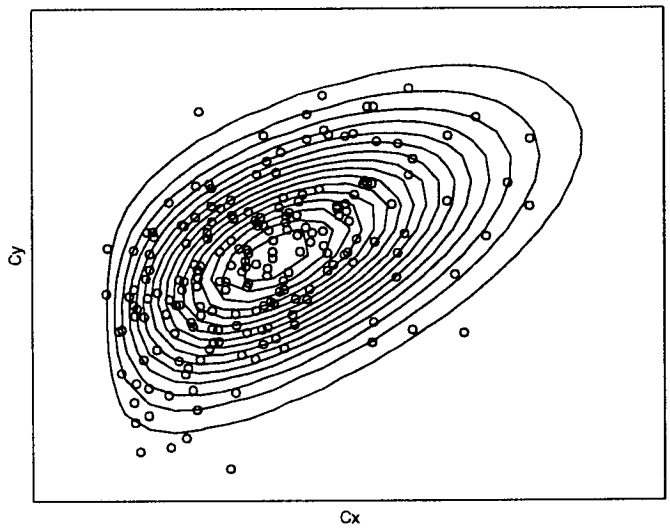

Fig. 2. A representative example for creating a sample of 200 particles using the procedure outlined in Fig. 1.

Although the method itself represents a general mathematical concept that is not new, the ability to carry it out for the Chapman-Enskog distribution is new because of the availability of Chou's analytic results. Even though the sampling procedure outlined above is considerably more efficient than the simple selection/rejection scheme, it is still fairly intensive and steps are being taken to reduce the computational effort still further. Some of these steps were taken by Duttweiler in creating a very efficient C program to implement the algorithm. Duttweiler's coding was used by Dahlby and by Lou in their respective thesis work.

V. Testing of a Flux-Based Hybrid Scheme

Considerable testing of a flux-based hybrid scheme was carried out by Lou for two nonsteady one-dimensional problems and by Dahlby for a steady two-dimensional problem. The first problem studied by Lou was the impulsively started piston, where the interface for the hybrid was placed at a fixed position 12.5 mean free path lengths ahead of the piston surface. Some of his results (taken from his thesis [4]) for the case of a monatomic gas and $M_{piston} = 1.0$ are shown in Fig. 3.

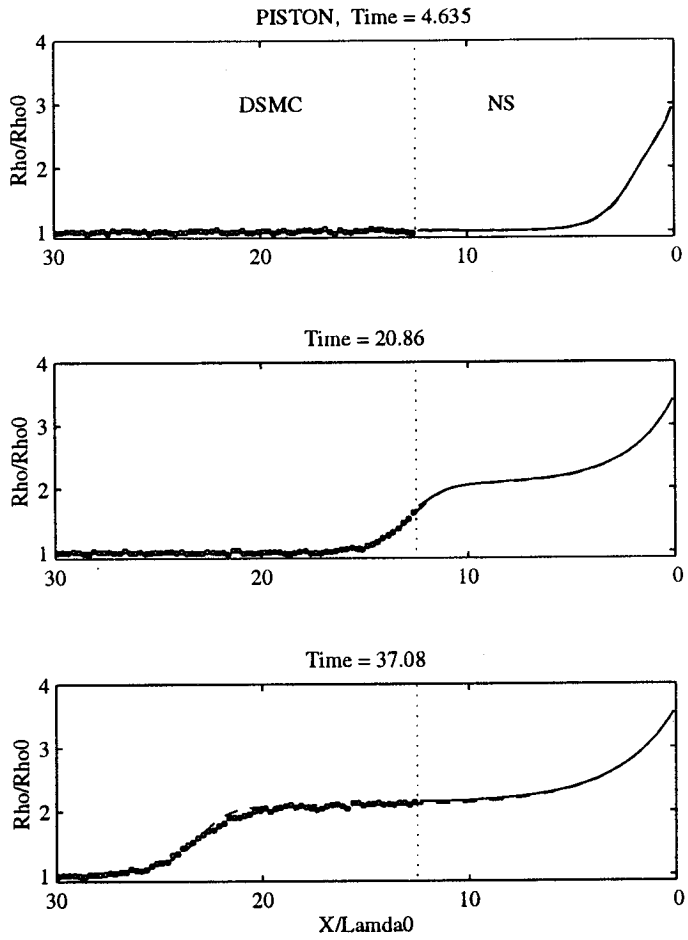

Fig. 3. A hybrid solution for an impulsively started piston, with the piston surface on the right, and the interface (dotted vertical line) at 12.5 mean free path lengths ahead of the piston. Dimensionless time is based on the upstream collision time.

The objective was to select conditions and a time scale for which one could observe

the wave front as it passed through the interface, to see if any imperfections appear at the point where the two solutions are joined. Far upstream and far downstream from the shock wave the conditions are essentially at equilibrium and no difficulty should be expected, but when the shock wave passes the interface location then severe nonequilibrium conditions are present, giving the matching algorithm its most severe test (intermediate time shown). Also shown in the figure, as a dashed curve, is a pure NS solution which is hardly distinguishable from the hybrid, indicating that the matching algorithm seems to be working rather well. For the later time shown, the hybrid arrangement is optimum for this problem, in that the shock wave profile itself can best be modeled by the DSMC method while the thermal layer at the piston surface can best be handled by the NS solution. The density profile for the intermediate time is quite similar in many respects to the density profile along the stagnation streamline in a supersonic flow past a blunt cold body, a situation of interest to us because it becomes a very useful application of the hybrid scheme.

The second problem studied by Lou was the impulsively started flat plate, where the interface for the hybrid was placed at a fixed position 10 mean free path lengths above the plate surface. Some of his results (taken from his thesis [4]) for the case of a monatomic gas and $M_{plate} = 1.0$ are shown in Fig. 4. Here again, the objective was to select conditions and a time scale for which one could observe the boundary layer as it grew and passed thought the interface, to see if any imperfections appeared at the point where the two solutions join. In this case the nonequilibrium was principally the result of stress with heat flux playing a lesser role. As can be seen, the matching again appears to be working very well. In this case it is also clear that the flux boundary conditions used in the KFVS method for the NS equations is accounting for velocity slip at the plate surface. The slip value is initially large and then diminishes as time progresses, reaching a level of about 10% for the latest time given.

For both the impulsively started piston and the impulsively started flat plate, the conditions were chosen so that a pure NS solution and a pure DSMC solution would predict the same results. This is possible as long as the Knudsen number is sufficiently small and the nonequilibrium is not too large. Because of this, we were free to place the interface at most any position in the hybrid solution (positioning was not critical); and we were always in a position to use either pure solution as a reference in judging the hybrid. In Lou's thesis [4] many of these comparisons are made, even

with a reversed DSMC/NS orientation. Also, in both cases it was necessary to study extremely short times in order for the nonequilibrium to be large, so that the hybrid scheme could be fully tested. Typically, a time of about 10 to 20 collision times was used, clearly a very short time in terms of physical processes.

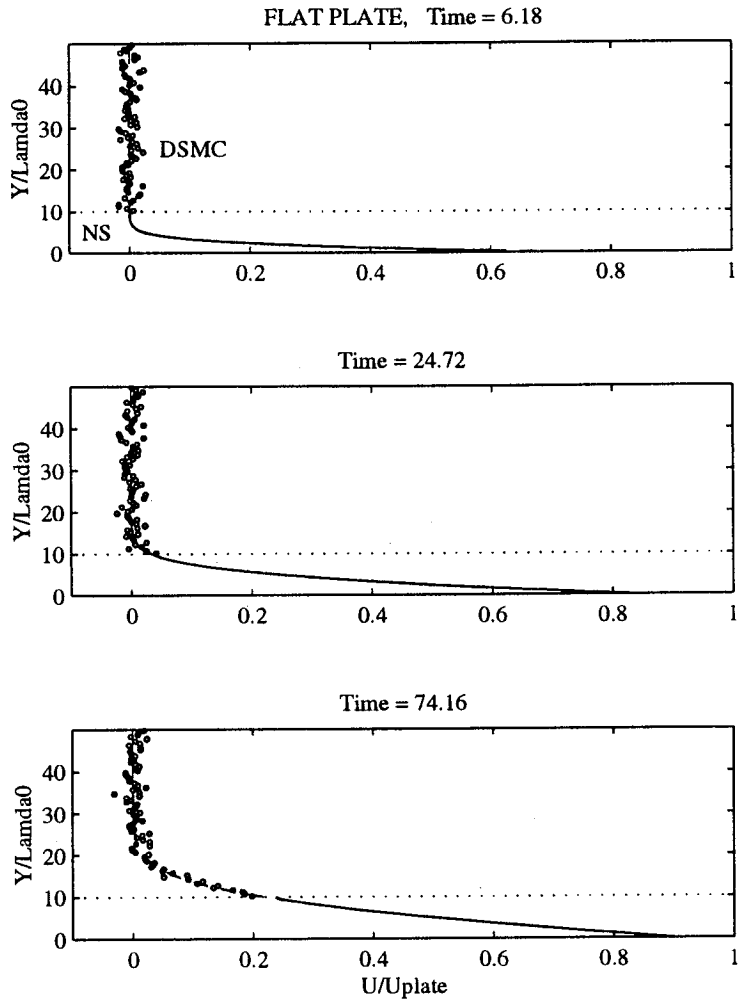

Fig. 4. A hybrid solution for an impulsively started flat plate, with the plate surface at the bottom, and the interface (indicated by the dotted horizontal line) at 10 mean free path lengths above the plate. Dimensionless time is based on the freestream collision time.

The third problem studied was the lid-driven cavity problem, or the slider plate problem. Large nonequilibrium develops in the two corners between the lid and the

cavity wall, and consequently, it is reasonable to assign the DSMC method a small strip alongside the lid, including the two corners; and then allow NS to handle the rest, where the degree of nonequilibrium is considerably smaller. The reason for this choice is that only DSMC alone can handle conditions where velocity slip and temperature slip may be large, and where the physical scale in the two corners may effectively lead to rarefied conditions. The hybrid solution for the pressure field is shown in Fig. 5, where the hybrid interface was placed at 50% of the depth of the cavity which can be visually located by the change in 'texture' of the surface.

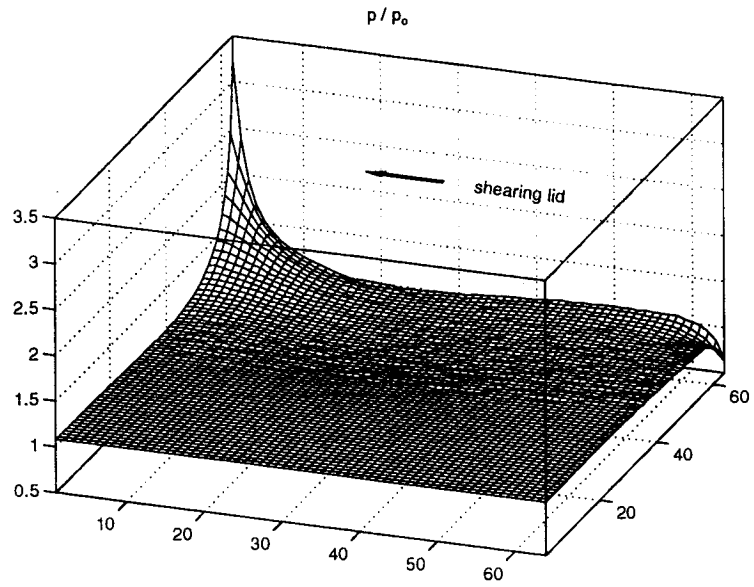

Fig. 5. A hybrid solution for the lid-driven cavity problem showing the pressure field for $Kn = 0.01$, $M_{lid} = 1.0$ and a monatomic gas. The shearing lid is on the far wall as indicated.

Because Dahlby carried out this study [3] at a fairly early point in our work, before we fully developed the means for sampling from the Chapman-Enskog velocity distribution function, he chose to place the interface at a position in the flow for which it was assured that nonequilibrium would be small, namely, the 50% location as shown. In this location, one is able to use the much simpler Maxwellian distribution, for which the proper sampling scheme is well known and straightforward. This test confirmed the intuitive view that there is a direct one-to-one correspondence between the degree of nonequilibrium present in the flow and the type of velocity distribution function needed to carry out the matching at a hybrid interface.

Because of the 'spiking' of the pressure field in the two corners, one is not able to tell whether the well-known singularity in stress and heat flux that appears for the no-slip solution of the NS equations has been eliminated. Shown in Fig. 6 is the u-component of the velocity, the component that lies parallel to the lid itself. In this case, the lid is located on the near face and moves from left to right in the figure.

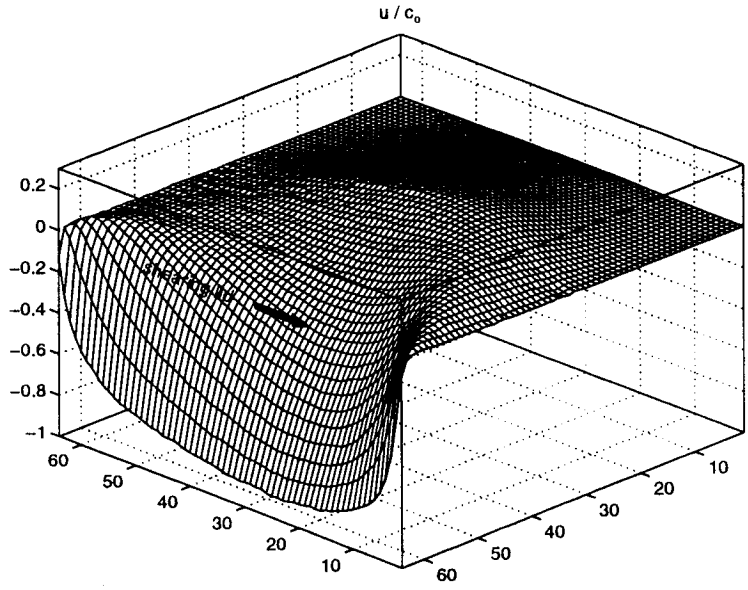

Fig. 6. A hybrid solution for the lid-driven cavity problem showing the component of the velocity lying parallel to the lid, for $Kn = 0.01$, $M_{lid} = 1.0$ and a monatomic gas. The shearing lid is on the near face as indicated.

The presence of velocity slip, seen in the figure as the difference between the plotted curve at the lid and the line at -1.0 indicating the Mach number of the lid, seems to have completely removed the infinite velocity gradient that otherwise appears in the two corners of the flow, and which leads to a singularity in stress when using the no-slip boundary condition.

VI. Capability for 2D/3D Simulations

Even though the lid-driven cavity problem represents two-dimensional flow, the interface used, consisting of a straight line, makes the interfacing effectively one

dimensional in terms of the spatial physics associated with the matching conditions. The next step in our work was to select a two-dimensional problem that required an interface that was also two dimensional. Such a case is shown in Fig. 7, which represents a supersonic flow past a rectangular prism.

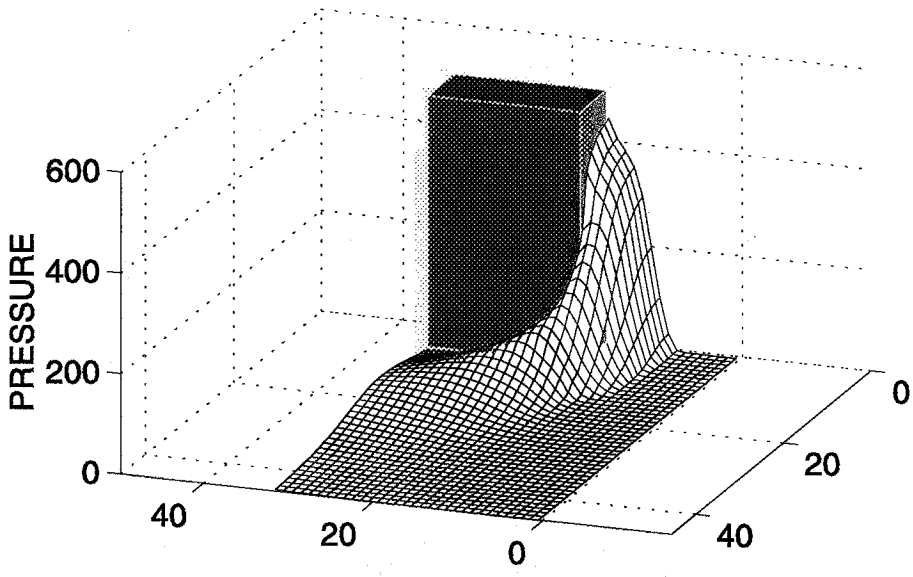

Fig. 7. A hybrid solution for Mach 16 flow over a rectangular prism, with NS shown in green and DSMC shown in blue.

As this represents our first effort, the location of the interface was not positioned properly. The forward location of the interface should not place the NS solution (shown in green) ahead of the shock wave, but should confine it to the region closer to the boundary layer. However, the purpose of the test was to provide the experience needed to handle a more complex interface and to demonstrate that our overall procedure was working properly. In this case the interface is a rectangular cutout with two sharp corners. The smooth transition seen in the figure between the NS solution and the DSMC simulation is what we had hoped to achieve before more complex testing was pursued. This work is being carried out by Duttweiler, as part of his thesis research, and a very preliminary report was presented by him at the CAS_96 Workshop [7].

At an earlier stage of our work, Dahlby was able to test the upper limit of our capability to study true 3D flows using a pure DSMC simulation. He designed a generic SSTO vehicle body, which could be placed at an arbitrary angle of attack,

and ran a series of simulations on the Intel Delta parallel supercomputer. A total of 1.1 million cells, 40 million particles, 512 nodes, 1000 sampling steps, and a run time of 110 minutes were used in each simulation. Figure 8 shows an example for 20^o angle of attack, free stream Mach number of 10, and a monatomic gas.

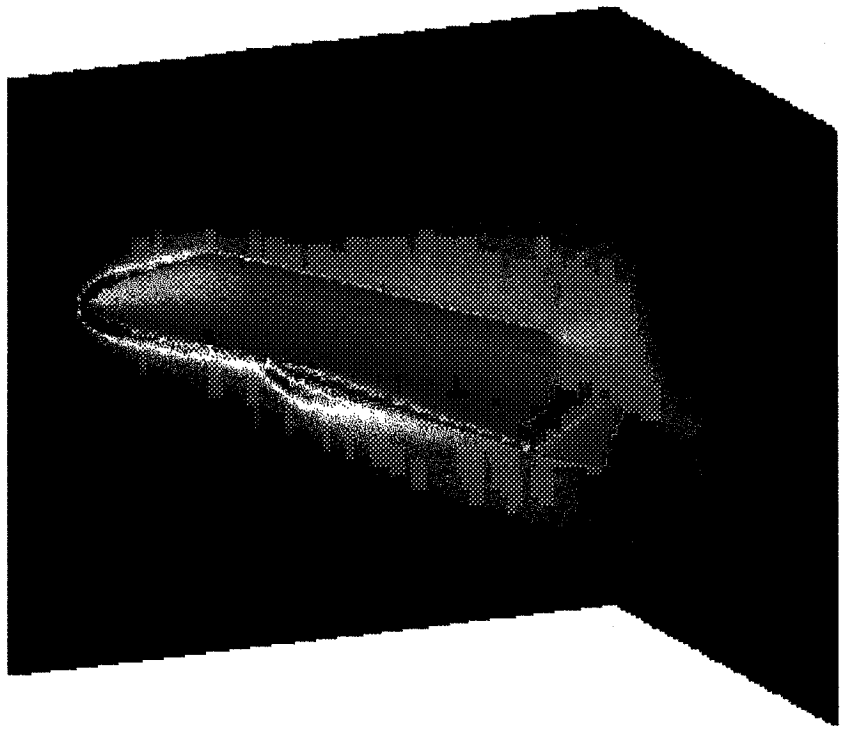

Fig. 8. Temperature distribution about a generic SSTO vehicle at 20^o angle of attack, $M_\infty = 10$, and for a monatomic gas.

Less than half of the available memory was committed because of concern that poor load balance may cause a processor to be assigned a series of spatial blocks containing more particles than the processor had memory to store. This would cause the over-allocated processor to report a memory error and exit the simulation, which in turn would cause all other processors to abort the simulation as well. By using on average only half of the available memory, there would be a negligible chance of over-allocating a single processor.

Dahlby was also able to conduct a number of interesting performance studies on our parallel code by using his generic SSTO body to represent a reasonably large problem. In one of his studies, he chose a simulation dimension of 120x120x120 for

a total of 1.7 million cells. This allowed him to evenly divide the simulation domain into cubical blocks of lengths 3, 4, 5, 6, 8, and 12 cells so that different runs could be carried out with a varying number of blocks per processor. Also, timing results were obtained with a total of 100 sampling time steps, as opposed to real runs of more than ten times greater. The aim was to study the effect on computation time of the tradeoff between the time required for load balancing, the final load balance state, and communication time. When there are only a few blocks per processor then the final load balance is poor because the apportionment of blocks is very restricted, and when the there are a large number of small blocks then communication cost and time to load balance become large. Figure 9 gives a summary of his findings. The most important observation made is that the histogram for the run-time data shows the minimum to be very broad, ranging from approximately 8 to 50 blocks per processor. The conclusion one draws from this is that, fortunately, most any reasonable engineering guess would turn out to be nearly optimum.

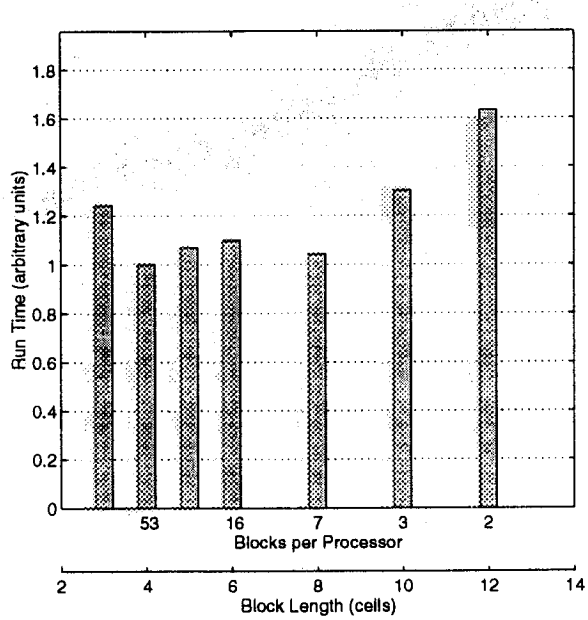

Fig. 9. Relative run time on the Intel Delta as a function of block size for the generic SSTO problem.

Considering our current capability to carry out 3D simulations with a large number of cells and a correspondingly large number of particles, we were interested in testing the limit of our resolution capability for a typical 2D problem. A circular cylinder was chosen for this test using a wind tunnel dimension of 576 cells by 896

cells for a total of 0.52 million cells; the number density was 16 particles per cell on average for a total of 8.3 million particles. The free stream Mach number was set to 10.95, the Knudsen number to 0.02, based on the cylinder radius, and the gas was monatomic. The temperature distribution about the cylinder is shown in Fig. 10.

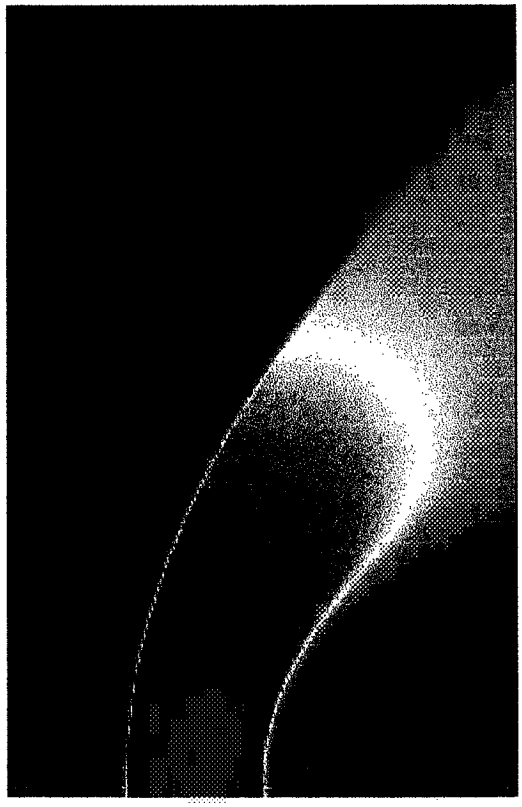

Fig. 10. Temperature distribution about a circular cylinder in a Mach 10.95 flow, monatomic gas and Kn = 0.02.

This DSMC simulation was used by Dahlby in his thesis as a reference solution in his study of the effect of cell size on the position of the shock wave and the thickness of the thermal boundary layer on the cylinder.

VII. DISCUSSION AND CONCLUSIONS

As shown by the following list of publications, our progress during the reporting period has been considerable. Most of the goals outlined in the introductory discussion have been met and clearly suggest that further effort along these lines could be

productively pursued. On this basis, our ongoing work has dealt with (1) questions related to more complex geometries in two and three dimensions, (2) further testing of matching conditions for these more complex geometries, (3) steps that could be taken to further reduce the computational load represented by the sampling needed to create new particles at the hybrid interface, (4) the introduction of grid refinement in the Navier-Stokes portion of the hybrid, and (5) studies of computational time associated with different approaches so that the best method can be identified.

PUBLICATIONS

1. Chou, S.Y., "Kinetic Flux Vector Splitting for the Navier-Stokes Equations," Ph.D. thesis, Stanford University, CA, June 1995.

2. Chou, S.Y. and Baganoff, D., "Kinetic Flux-Vector Splitting for the Navier-Stokes Equations," Journal of Computational Physics, to be published.

3. Dahlby, D.C., "Methods of Optimization for Running Large 2D/3D Particle Simulations on a Parallel Supercomputer," Ph.D. thesis, Stanford University, CA, December 1995.

4. Lou, T., "Basis for a Hybrid Scheme Combining Kinetic Flux Vector Splitting for the Navier-Stokes Equations with a Particle Method", Ph.D. thesis, Stanford University, CA, December 1996, to be published.

5. Lou, T., Dahlby, D.C., and Baganoff, D., "A Numerical Study Comparing Kinetic Flux-Vector Splitting for the Navier-Stokes Equations with a Particle Method," Journal of Computational Physics, submitted.

6. Dahlby, D.C, Fallavollita, M.A., and Baganoff, D., "Performance and Optimization of a Parallel Implementation of a Particle Method for Simulating 3D Rarefied Flow," Computational Aerosciences Workshop 95, NASA CD Conference Publication 20010, p. 126, January, 1996.

7. Duttweiler, C.R., Dahlby, D.C, and Baganoff, D., "Parallel Implementation of a Hybrid Navier-Stokes/Particle Method for Simulating Rarefied Flow," Computational Aerosciences Workshop 96, NASA CD Conference Publication, to be published.

APPENDIX A

Kinetic Flux-Vector Splitting for the Navier-Stokes Equations

S. Y. Chou and D. Baganoff
Department of Aeronautics and Astronautics
Stanford University, Stanford, CA 94305
(Submitted to: Journal of Computational Physics, Oct. 4, 1995; Revs: Feb. 26, May 24, 1996)

Before a hybrid scheme can be developed combining the direct simulation Monte Carlo (DSMC) method and a Navier-Stokes (NS) representation, one must have access to compatible kinetic-split fluxes from the NS portion of the hybrid scheme. The kinetic theory basis is given for the development of the required fluxes from the Chapman-Enskog velocity distribution function for a simple gas; and these are then extended to a polyatomic gas by use of the Eucken approximation. The derived fluxes are then used to implement boundary conditions at solid surfaces that are based on concepts associated with kinetic theory and the DSMC method. This approach is shown to lead to temperature slip and velocity slip as a natural outcome of the new formulation, a requirement for use in the near-continuum regime where DSMC and NS must be joined. Several different flows, for which solid boundaries are not present, are computed using the derived fluxes together with a second-order finite-volume scheme and the results are shown to agree well with several established numerical schemes for the NS equations.

I. INTRODUCTION

A question that frequently arises when attempting to model plume flows generated by thrusters operating in the vacuum of space is: how to interface a numerical solution of the Navier-Stokes (NS) equations, which is most appropriate for the high-density gas flow found inside a nozzle, with the direct simulation Monte Carlo (DSMC) method [2], which is most appropriate for modeling the very low-density gas flow found in the outer plume? A similar question arises for the case of a blunt body in a rarefied high-enthalpy flow, where a numerical solution of the NS equations is often the most appropriate for handling the high-density gas layer found near the relatively cold body surface, while the DSMC method is the most appropriate for the rarefied outer flow.

Both questions can best be understood by considering the much simpler case of an impulsively started piston in a stationary gas, where the piston travels in a direction normal to its surface, the piston Mach number is assumed high, and the piston temperature and gas temperature are initially equal. A NS solution for a representative case is shown in Fig. 1, where the piston Mach number is taken to be 5.0 and the gas to be ideal and monatomic. A normal shock wave forms ahead of the piston, the gas temperature (dashed curve) rises behind the shock and then falls as a result of the cold piston surface (located at $x/L = 1$). Because of the nearly constant pressure between the shock and the piston, the density (solid curve) rises in the thermal layer in an inverse ratio to the temperature. In this case, the peak density is 8.2 times the density behind the shock wave. Although the DSMC method must be used to obtain the proper shock wave profile, as is well known, it is clear that the much higher density in the thermal layer would lead to a greatly increased DSMC simulation cost in that region, prompting consideration of a hybrid scheme, where the DSMC method would be used to model the outer flow and the NS equations to model the thermal layer. This concept is schematically depicted in Fig. 2.

Because the DSMC method is based on kinetic theory, the DSMC fluxes to be matched at an interface of a hybrid solution are physical quantities: the fluxes emanating from the DSMC region F^+ are one-sided kinetic fluxes and the frame of reference is an inertial frame, as indicated in Fig. 2. The flux of mass (momentum or energy) from the DSMC side is gotten directly from the particles that cross the interface in one time step. In order to develop an effective hybrid scheme, one must therefore address the following issues.

- The same definitions should be used for the split fluxes when matching at an interface, preferably the kinetic theory definition of one-sided kinetic fluxes (DSMC) in an inertial frame of reference.
- As indicated by Figs. 1 and 2, considerable nonequilibrium may exist at an interface in the form of heat flux or shearing stress when considering a boundary-layer flow. Therefore, the numerical scheme chosen to interface with DSMC must solve the NS equations; and because the DSMC method possesses characteristics of a time-dependent finite-volume scheme, compatibility suggests the use of the same scheme for the NS portion.
- Because matching can only be carried out in the near-continuum regime, where both DSMC and NS are valid, it is clear that velocity slip and/or temperature slip would be present at the body surface, i.e., the piston surface in Fig. 2. Therefore, the NS solution must account for slip; the no-slip boundary condition cannot be used.

- The numerical scheme handling the NS portion must be shown to agree with existing numerical methods for the NS equations before a hybrid scheme is constructed.
- Conversion of the NS values for the one-sided kinetic fluxes at an interface into a corresponding collection of particles for insertion into the DSMC simulation must be carried out in a physically compatible and computationally cost effective way.
- Conditions must be identified that define a suitable location for placement of an interface. For example, for moderate nonequilibrium, it is generally found that good results are obtained for DSMC simulations if the local cell Knudsen number (local mean free path length to cell dimension) is greater than unity. To use this criterion, questions of compatibility with the NS equations would have to be explored.
- Both the NS scheme selected and the resultant hybrid scheme created must be compared with different DSMC solutions for complete verification.

The objective of the present study is to address and discuss the first four issues listed above; the remaining three will be covered in follow-on reports.

Much of the groundwork for the present investigation can be found in a book by Patterson [13] and in papers by Broadwell [4], Bird [2], Pullin [15], Prendergast & Xu [14], Mandal & Deshpande [12], and Gooch [8]. Because we seek a formulation based on the NS equations, and because much of the previous work focused on the Euler equations, it is appropriate to first turn to general results found in work on kinetic theory, in particular, the well-known system of moment equations formed from the Boltzmann equation. This approach treats the equilibrium and nonequilibrium components of the fluxes on the same footing, and the derivation itself provides the definitions along with the justification for their use. An alternative is the separate introduction of the nonequilibrium terms at the macroscopic level, as discussed by Macrossan & Oliver [10] and by Mallett et al. [11], but this approach would not directly satisfy the first and fifth condition in the above list of issues.

II. MOMENTS OF THE BOLTZMANN EQUATION

Many of the equations and concepts to be presented in this section can be found in standard work on kinetic theory, such as Chapman & Cowling [5], Grad [9], Patterson [13], Vincenti & Kruger [20], Woods [22], and Bird [3]. We start with the case of an ideal monatomic gas in the absence of external forces and assume the gas is sufficiently dilute for binary collisions to dominate. For this case, the Boltzmann equations reads

$$\frac{\partial(nf)}{\partial t} + c_k \frac{\partial(nf)}{\partial x_k} = \left[\frac{\partial(nf)}{\partial t}\right]_{coll}, \tag{1}$$

where n is the number density, f is the velocity distribution function, c_k the molecular velocity in an inertial frame, the repeated index k denotes a sum, and the right-hand side represents the collision integral. The moment equations are obtained by multiplying the Boltzmann equation by any function of molecular velocity $Q(c_i)$ and integrating over velocity space. These equations are represented by

$$\frac{\partial}{\partial t}(n < Q >) + \frac{\partial}{\partial x_k}(n < c_k Q >) = \Delta[Q]. \tag{2}$$

The two operators appearing in (2) are defined by

$$< Q >= \int_{-\infty}^{\infty}\int_{-\infty}^{\infty}\int_{-\infty}^{\infty} Q f dc_1 dc_2 dc_3 \tag{3}$$

and

$$\Delta[Q] = \int_{-\infty}^{\infty}\int_{-\infty}^{\infty}\int_{-\infty}^{\infty} Q \left[\frac{\partial(nf)}{\partial t}\right]_{coll} dc_1 dc_2 dc_3. \tag{4}$$

When the arbitrary function of molecular velocity $Q(c_i)$ is chosen to be one of the five collisional invariants $Q^{INV} = m\{1,\ c_i,\ c^2/2\}$, where m is the molecular mass and c^2 represents the square of the velocity magnitude, then the corresponding moment of the collision integral is identically zero, i.e., $\Delta[Q^{INV}] = 0$. This is a general result that

holds for any distribution function f and for any molecular interaction law. This selection leads to the conservation laws for gas dynamics, which can be written in the form

$$\frac{\partial}{\partial t}(n < Q^{INV} >) + \frac{\partial}{\partial x_k}(n < c_k Q^{INV} >) = 0, \tag{5}$$

or, when using each of the collisional invariants in turn, one obtains the set

$$\frac{\partial}{\partial t}(\rho) + \frac{\partial}{\partial x_k}(\rho < c_k >) = 0 \tag{6a}$$

$$\frac{\partial}{\partial t}(\rho < c_i >) + \frac{\partial}{\partial x_k}(\rho \langle c_k c_i \rangle) = 0 \tag{6b}$$

$$\frac{\partial}{\partial t}(\rho < c^2/2 >) + \frac{\partial}{\partial x_k}(\rho < c_k c^2/2 >) = 0, \tag{6c}$$

where $\rho = mn$ is the mass density.

Introduction of the thermal velocity components $C_i = (c_i - u_i)$, where $u_i =< c_i >$ is the mean or fluid velocity, allows one to introduce the central moments defined by

$$P_{ij} = \rho < C_i C_j > \tag{7}$$

$$p = P_{kk}/3 \tag{8}$$

$$\tau_{ij} = -P_{ij} + p\delta_{ij} \tag{9}$$

$$e =< C^2/2 > \tag{10}$$

$$q_i = \rho < C_i C^2/2 >, \tag{11}$$

where P_{ij} is the pressure tensor or stress tensor, p the pressure, τ_{ij} is the viscous stress tensor, e is the internal energy (translational) for a monatomic gas, and q_i is the heat flux vector for a monatomic gas. The conservation laws for gas dynamics can then be written in the familiar form

$$\frac{\partial}{\partial t}(\rho) + \frac{\partial}{\partial x_k}(\rho u_k) = 0 \tag{12a}$$

$$\frac{\partial}{\partial t}(\rho u_i) + \frac{\partial}{\partial x_k}(\rho u_k u_i + P_{ki}) = 0 \tag{12b}$$

$$\frac{\partial}{\partial t}\left[\rho\left(e + \frac{u^2}{2}\right)\right] + \frac{\partial}{\partial x_k}\left[\rho u_k\left(e + \frac{u^2}{2}\right) + P_{ki}u_i + q_k\right] = 0. \tag{12c}$$

If the gas is not simply a monatomic gas but has internal structure, then the above procedure must be modified. Because the general problem includes the question of what equation replaces (1), the problem is rather difficult and it becomes necessary to make use of a suitable approximation. One simplistic approach is to assume that all internal molecular energy modes are in equilibrium, both internally and with the translational degrees of freedom. Thus, the additional internal energy e_{int} can be expressed in terms of the translational temperature T by the equilibrium relation

$$e_{int} = \frac{1}{2}\left(\frac{5 - 3\gamma}{\gamma - 1}\right) RT, \tag{13}$$

where R is the gas constant, and where an accounting for the additional internal energy is introduced through the ratio of specific heats γ, and for which $e_{int} = 0$ in the case of a monatomic gas.

To properly account for the amount of energy that is carried by a particle with internal structure, the energy $mc^2/2$ must be replaced by $(mc^2/2 + \epsilon)$, where ϵ is the additional internal energy per particle, and therefore, the quantities of interest become

$$Q^{INV} = \{m,\ mc_i,\ (mc^2/2 + \epsilon)\}\,. \tag{14}$$

Assuming Eq. (1) continues to hold for the extended distribution function $f(c_i, \epsilon)$ and provided the right-hand side is interpreted in a suitable way, then an additional integral over ϵ is formally required in applying both (3) and (4). It is reasonable to argue, however, that the quantities in (14) must continue to be conserved in a collision, and consequently, (4) again evaluates to zero; and thus, (5) remains unchanged.

In evaluating the left-hand side of (5) for the five different quantities in (14), identical results to those obtained for the monatomic gas will be found for all quantities that contain polynomials in c_i alone. This follows from the fact that integration over the ϵ variable can be taken first and independently from the c_i integration. Therefore, Eqs. (6a) and (6b), and consequently (12a) and (12b), are fully recovered. The same conclusion also applies to the first term in the quantity $(mc^2/2 + \epsilon)$ and therefore (6c) is replaced by

$$\frac{\partial}{\partial t}(\rho < c^2/2 > + n < \epsilon >) + \frac{\partial}{\partial x_k}(\rho < c_k c^2/2 > + n < c_k \epsilon >) = 0. \tag{15}$$

Substitution of the central moments (7)-(11) into (15) reproduces all of the previous algebra for the monatomic gas and leads to

$$\frac{\partial}{\partial t}\left[\rho\left(e + \frac{u^2}{2}\right) + \rho e_{int}\right] + \frac{\partial}{\partial x_k}\left[\rho u_k\left(e + \frac{u^2}{2}\right) + P_{ki}u_i + q_k + (n < C_k \epsilon > + \rho u_k e_{int})\right] = 0, \tag{16}$$

where the definition $< \epsilon >= m e_{int}$ has been used. Therefore (12c) also continues to hold provided we replace (10) by

$$e = (< C^2/2 > + e_{int}) \tag{17}$$

and the definition of the heat flux vector (11) by

$$q_i = \rho < C_i C^2/2 > + n < C_i \epsilon > . \tag{18}$$

We therefore conclude that the complete collection of equations (5), (6) and (12) can be used as they stand, provided definitions (17) and (18) are employed when the gas possesses internal structure, and a state of equilibrium exists between the internal modes and the translational degrees of freedom (see [20], p. 326).

Because the conservation equations (12) can be developed for any general fluid through use of phenomenological arguments alone, the set is actually more general than the kinetic theory derivation would indicate, i.e., they are also the conservation equations for fluid dynamics. However, we are only interested in treating an ideal gas flow and the use of the kinetic theory approach is necessary because it shows that the set is valid for any degree of translational nonequilibrium, that is, for any translational velocity distribution function one cares to consider. If one chooses the equilibrium distribution, namely the Maxwellian distribution f^{Max}, then the set becomes the Euler equations, because viscous stress and heat flux are identically zero for f^{Max}. This step allows one, in effect, to reproduce the special case considered by Pullin [15] in his equilibrium flux method (EFM), as well as the work by Mandal & Deshpande [12], on kinetic flux-vector splitting (KFVS) for the Euler equations. The inviscid limit of the recent work by Mallett et al. [11] is also recovered by this step. If one chooses a Chapman-Enskog (CE) distribution f^{CE}, then the set becomes the Navier-Stokes equations, because stress and heat flux are then given by the corresponding Chapman-Enskog expressions. This is the path that we will follow in developing a KFVS scheme for the NS equations. One may also choose a discrete representation for f and the equations still hold. This is an alternate interpretation of the concept that lies behind the state vector splitting scheme for the Navier-Stokes equations introduced by Gooch [8]. The most important point is that one is free to choose any translational velocity distribution function whatsoever in using Eqs. (5), (6) or (12); and in so doing, the set becomes closed, as long as f is fully specified. Otherwise, if f remains general, then one is faced with the well-known closure problem, when using a moment method, because τ_{ij} and q_i are then unknown quantities in the equations. It is useful to emphasize the fact that the conservation equations as displayed in (12) are not the NS equations until one introduces f^{CE}.

Each of the five separate moment equations represented by either (5), (6) or (12) can be expressed by the single form

$$\frac{\partial U}{\partial t} + \frac{\partial F_k}{\partial x_k} = 0. \tag{19}$$

The complete specification of F_i in three dimensions, as defined by (19), requires the evaluation of 15 quantities. But the task is made considerably simpler, if one considers a finite volume scheme, uses Gauss' divergence theorem, and writes Eq. (19) as

$$\frac{\partial}{\partial t}\int_V U dV + \int_S F_n dS = 0, \tag{20}$$

where S encloses the volume V and F_n is the projection of F_i onto the unit outward pointing normal for the surface element dS. If V is taken to be a rectangular volume, then one only needs to evaluate five quantities for each planar surface, a conceptually simpler task provided F_n can be evaluated directly. Using the notation of (5), we then have

$$U = n < Q^{INV} > \tag{21}$$

and

$$F_n = n < c_n Q^{INV} >, \tag{22}$$

where U is the state vector, F_n is the total flux vector, and c_n is the component of the molecular velocity normal to the planar surface. Equation (22) clearly represents a physical concept. This can be seen from the fact that Q is a scalar quantity which is carried across the fixed surface by c_n, thus creating a physical flux in that quantity.

The five fluxes defined by (22) are total fluxes, not the one-sided fluxes depicted in Fig. 2. In addition, these general expressions contain both the inviscid fluxes as well as the nonequilibrium components due to viscous stress and heat flux, as can be seen from the corresponding terms in (12). Because many quantities evaluate to zero in arriving at the set (12), and these cannot be recovered in a simple way, one must use the more primitive set (5), or (6), in developing the algebra for the one-sided, kinetic-split fluxes.

III. KINETIC SPLIT FLUXES

As seen in Fig. 2, we are interested in expressions for the one-sided fluxes based on a fixed interface and an inertial frame of reference. On this basis and on considering the x_1 direction as positive, we can split the integration in c_1 as follows

$$\begin{aligned}\int_{-\infty}^{\infty}\int_{-\infty}^{\infty}\int_{-\infty}^{\infty}\{....\}\,dc_1dc_2dc_3 &= \int_{-\infty}^{\infty}\int_{-\infty}^{\infty}\left(\int_{-\infty}^{0}+\int_{0}^{\infty}\right)\{....\}\,dc_1dc_2dc_3 \\ &= \int_{-\infty}^{\infty}\int_{-\infty}^{\infty}\left(\int_{-\infty}^{-u_1}+\int_{-u_1}^{\infty}\right)\{....\}\,dC_1dC_2dC_3,\end{aligned} \tag{23}$$

where the second expression introduces the thermal velocity components C_i. The concept of a kinetic split flux has a long history in kinetic theory and a clear application to an equilibrium flow can be found in a textbook by Patterson (Ref. [13], pp. 163-167). On using the following notation to represent the splitting in (23)

$$F = F^- + F^+, \tag{24}$$

and on introducing a Cartesian coordinate system $(n, t1, t2)$ located in an arbitrary fixed planar surface, we obtain from (22), (23) and (24) the definitions

$$F_n^- = n\int_{-\infty}^{\infty}\int_{-\infty}^{\infty}\int_{-\infty}^{-u_n}(C_n+u_n)Q^{INV}f dC_n dC_{t1}dC_{t2} \tag{25}$$

$$F_n^+ = n\int_{-\infty}^{\infty}\int_{-\infty}^{\infty}\int_{-u_n}^{\infty}(C_n+u_n)Q^{INV}f dC_n dC_{t1}dC_{t2} \tag{26}$$

These relations provide the means for computing F_n when f is a known function.

Because the total fluxes are known from the terms in (12), explicit expressions for each of the collisional invariants given by (14) need only be listed for, say, F_n^+. It is also useful to introduce a more physically descriptive notation for the split fluxes as follows.

$$F^+_{zero} = \int_{-\infty}^{\infty}\int_{-\infty}^{\infty}\int_{-u_n}^{\infty} f dC_n dC_{t1} dC_{t2} \tag{27}$$

$$F^+_{mass} = \rho \int_{-\infty}^{\infty}\int_{-\infty}^{\infty}\int_{-u_n}^{\infty} (C_n + u_n) f dC_n dC_{t1} dC_{t2} \tag{28}$$

$$F^+_{n-mom} = \rho \int_{-\infty}^{\infty}\int_{-\infty}^{\infty}\int_{-u_n}^{\infty} (C_n + u_n)^2 f dC_n dC_{t1} dC_{t2} \tag{29}$$

$$F^+_{t1-mom} = \rho \int_{-\infty}^{\infty}\int_{-\infty}^{\infty}\int_{-u_n}^{\infty} (C_n + u_n)(C_{t1} + u_{t1}) f dC_n dC_{t1} dC_{t2} \tag{30}$$

$$F^+_{tr-energy} = \rho \int_{-\infty}^{\infty}\int_{-\infty}^{\infty}\int_{-u_n}^{\infty} (C_n + u_n)\left[(C_n + u_n)^2 + (C_{t1} + u_{t1})^2 + (C_{t2} + u_{t2})^2\right] \times \frac{1}{2} f dC_n dC_{t1} dC_{t2} \tag{31}$$

$$F^+_{int-energy} = n \int_0^{\infty}\int_{-\infty}^{\infty}\int_{-\infty}^{\infty}\int_{-u_n}^{\infty} (C_n + u_n)\epsilon f dC_n dC_{t1} dC_{t2} d\epsilon = \Delta q^+_{Eucken} + \rho u_n e^+_{int} \tag{32}$$

$$F^+_{energy} = F^+_{tr-energy} + F^+_{int-energy}. \tag{33}$$

Integration over the ϵ variable is not shown in Eqs. (27)-(31) because it can be carried out as an independent operation and done first. However, it does appear explicitly in (32), and this equation must be included when a gas has internal structure. The role played by (32) can be seen from the fact that the $C_n\epsilon$ term in the integrand is the source of the second term in (18), while the $u_n\epsilon$ term is the source of the second term in (17). The difficulty in applying (32) results from the fact that we need an explicit expression for the joint distribution $f(C_i, \epsilon)$ in order to evaluate these split fluxes; and this lack of knowledge is indicated by the notation employed following the second equality. However, in the case of the total e_{int}, it is given by (13) since our model assume equilibrium for the internal degrees of freedom. Likewise, for the total flux represented by Δq_{Eucken}, we can use the Eucken model which replaces $< C_n\epsilon >$ by a quantity that is proportional to the temperature gradient, thus making it proportional to the heat flux vector (see [22], p. 66]). The net effect changes the value of the coefficient of thermal conductivity, as well as the Prandtl number, from that for a simple gas to the proper values for a gas with internal structure. This then allows one to use the same basic relations found for a simple gas. We will use the Eucken approximation and represent the incremental contribution to the heat flux due to the internal degrees of freedom by

$$\Delta q_{Eucken} = \Delta q^-_{Eucken} + \Delta q^+_{Eucken} = -K'' \nabla T. \tag{34}$$

These steps alone, however, still do not answer the question of how one evaluates the split fluxes appearing in (32). This will be done after we have completed the implementation of the Eucken model.

The extra quantity F^+_{zero} is also listed because it defines how the velocity distribution function itself is split, which is needed in the overall algebra. This can be seen from the normalization condition $F_{zero} = F^-_{zero} + F^+_{zero} = 1$ for a probability distribution. The expression for F^+_{t2-mom} is not listed because it can be gotten by merely interchanging $t1$ and $t2$ in (30). For a monatomic gas, the set of equations is very general and applies for any velocity distribution function one cares to define, for example, even for a discrete distribution. For a polyatomic gas, the set is not quite as general and is limited by the Eucken model and the approximations to be introduced below. Our interest is in the Chapmann-Enskog distribution and the resulting split fluxes.

IV. CHAPMAN-ENSKOG SPLIT FLUXES

A gas flow that is in thermodynamic equilibrium is represented locally by a Maxwellian distribution, and a gas flow that is slightly disturbed from the equilibrium state is represented locally by the Chapman-Enskog distribution. The

CE distribution is obtained as an approximate solution of the Boltzmann equation (for a simple gas) and is expressed as a product of a local Maxwellian and a polynomial function of the thermal velocity components C_i, that is, by the relation

$$f^{CE} = f^{Max}(1 + \phi_1 + \phi_2) \tag{35}$$

where

$$f^{Max} = (2\pi RT)^{-3/2} exp\left(-C^2/2RT\right)$$
$$\phi_1 = -\left(\frac{\rho}{p^2}\right)\left(K^{(1)}\frac{\partial T}{\partial x_k}\right) C_k\left(C^2/5RT - 1\right)$$
$$\phi_2 = -\left(\frac{\rho}{p^2}\right)\left(\mu^{(1)}\frac{\partial u_j}{\partial x_k}\right)\left(C_jC_k - \frac{1}{3}C^2\delta_{jk}\right),$$

and where $K^{(1)}$ is the coefficient of thermal conductivity and $\mu^{(1)}$ the coefficient of viscosity as determined by the first-order Chapmann-Enskog procedure, and δ_{jk} the Kronecker delta. Because both the temperature gradient and the velocity-gradient tensor appear as parameters in f^{CE}, notational efficiency can be gained in the algebra that follows by replacing those quantities by the Chapman-Enskog expressions for stress and heat flux, i.e., by

$$q_i^{CE} = -K^{(1)}\frac{\partial T}{\partial x_i} \tag{36}$$

$$\tau_{ij}^{CE} = \mu^{(1)}\left(\frac{\partial u_i}{\partial x_j} + \frac{\partial u_j}{\partial x_i}\right) - \frac{2}{3}\mu^{(1)}\left(\frac{\partial u_k}{\partial x_k}\right)\delta_{ij}. \tag{37}$$

At this point we face a logical difficulty. Must we fix the Prandtl number to the value for a simple gas ($Pr = \mu^{(1)}c_p/K^{(1)} = 2/3$) or may we allow it to vary so that (36) becomes consistent with the Eucken approximation? As there is no simple answer, we will defer the question to the point in the analysis where logical conflicts can be more easily identified. On substituting (35) into Eqs. (27)-(31) and using the same orthogonal coordinate system $(n, t1, t2)$, we see that in each case the integrand becomes a product of polynomials in the thermal velocities C_i and the Maxwellian distribution f^{Max}. The only difficulty that appears in carrying out the integration is the large number of terms that are produced. For example, ϕ_1 and ϕ_2 are composed of 4 and 9 terms, respectively, and therefore (35) leads to a total of 14 terms. On evaluating $F^+_{tr-energy}$ alone, we are faced with 252 terms. This at first appears to be an overwhelming task, until it is noticed that many of the terms are zero, because in the C_{t1} and C_{t2} variables all odd moments of the symmetric function f^{Max} are zero and even moments are well-known functions of RT. Likewise, integration in the C_n component can be handled by splitting the integration into $-u_\infty$ to 0 + 0 to ∞ which then leads to exponential and error functions (see [3], p. 417). Because the collection of functions is small, there is hope the results can be finally assembled into fairly compact expressions. Even though the details are daunting, Patterson (Ref. [13], p. 77) used a method he reports was "initiated by Maxwell and developed by Chapman" to develop general expressions for the total fluxes, for the case of nonisentropic flow, which employs concepts and algebra very similar to that employed here. Our interest, however, is in obtaining the split fluxes for which many more terms must be handled. To carry out the present study, intensive use of symbolic mathematical manipulations, provided by MATHEMATICA, was made in handling the algebra. Only the final collected integrated results will be presented here. A discussion of the detailed steps required to obtain the following relations can be found in [6].

$$F^{\pm}_{zero} = \frac{1}{2}\left[(1 \pm \alpha_1) \pm \alpha_2\left(S_n\hat{\tau}^{CE}_{nn} + (2S_n^2 - 1)\hat{q}^{CE}_n\right)\right] \tag{38}$$

$$F^{\pm}_{mass} = \rho\sqrt{RT/2}\left[(1 \pm \alpha_1)S_n \pm \alpha_2(1 - \chi_1)\right] \tag{39}$$

$$F^{\pm}_{n-mom} = p\left[(1 \pm \alpha_1)\left(S_n^2 + \frac{1}{2}(1 - \hat{\tau}^{CE}_{nn})\right) \pm \alpha_2\left(S_n + \hat{q}^{CE}_n\right)\right] \tag{40}$$

$$F^{\pm}_{t1-mom} = \sqrt{2RT}\left[S_{t1}F^{\pm}_{mass}\right] + \frac{1}{2}p\left[-(1 \pm \alpha_1)\hat{\tau}^{CE}_{nt1} \pm \alpha_2\hat{q}^{CE}_{t1}\right] \tag{41}$$

$$F^{\pm}_{tr-energy} = p\sqrt{RT/2}\left[(1 \pm \alpha_1)\left(S_n(\frac{5}{2} + S^2) + \chi_2\right) \pm \alpha_2\left(2 + S^2 + \chi_3\right)\right] \tag{42}$$

$$F^{\pm}_{int-energy} = (\Delta q^{\pm}_{Eucken} + \rho u_n e^{\pm}_{int}) = \frac{1}{2}\left(\frac{5-3\gamma}{\gamma-1}\right)\left[RTF^{\pm}_{mass}\right] \tag{43}$$

$$F^{\pm}_{energy} = F^{\pm}_{tr-energy} + F^{\pm}_{int-energy}, \tag{44}$$

where

$$\begin{aligned}
&\alpha_1 = erf(S_n), \qquad \alpha_2 = \frac{1}{\sqrt{\pi}}e^{-S_n^2} \\
&\chi_1 = \left[S_n \hat{q}_n^{CE} + \frac{1}{2}\hat{\tau}_{nn}^{CE}\right] \\
&\chi_2 = \left[\frac{5}{2}\hat{q}_n^{CE} - \left(S_n\hat{\tau}_{nn}^{CE} + S_{t1}\hat{\tau}_{nt1}^{CE} + S_{t2}\hat{\tau}_{nt2}^{CE}\right)\right] \\
&\chi_3 = \left[S_{t1}\hat{q}_{t1}^{CE} + S_{t2}\hat{q}_{t2}^{CE} - \chi_1\left(1 + S_{t1}^2 + S_{t2}^2\right) - \hat{\tau}_{nn}^{CE}\right] \\
&S_n = u_n/\sqrt{2RT}, \qquad S^2 = S_n^2 + S_{t1}^2 + S_{t2}^2 \\
&\hat{\tau}_{nn}^{CE} = \tau_{nn}^{CE}/p, \qquad \hat{q}_n^{CE} = \frac{2}{5}q_n^{CE}/(p\sqrt{2RT}).
\end{aligned}$$

Each individual component of S_i, $\hat{\tau}_{ij}$ and $\hat{q}_i$ is not listed, as they are clearly nondimensionalized the same way.

Equations (38)-(42) are not outwardly affected by the physics associated with additional internal degrees of freedom, i.e., $\gamma \neq 5/3$. In view of this, these equations should not contain γ explicitly, when expressed appropriately. This is easily done by introducing the speed ratio $S = u/\sqrt{2RT}$, which is frequently used in kinetic theory, as opposed to the Mach number, which requires the introduction of γ through the isentropic speed of sound. Use of the speed ratio S not only provides a useful physical check on the mathematical results, it also allows the final expressions to be written in a more compact form. On the other hand, the physical concepts that lead to (43) directly involve additional internal degrees of freedom and the relation should contain γ explicitly, which is seen in the expression that follows the second equality, a step to be explained in the following discussion.

It is appropriate to review several consistency checks on Eqs. (38)-(43). First, the total fluxes (24) should agree with the corresponding expressions in (12). Starting with (38), we have $F_{zero} = 1$, which is the correct normalization condition for a probability distribution. From (39)-(43), we have

$$F_{mass} = \rho u_n \tag{45}$$

$$F_{n-mom} = \rho u_n^2 + p - \tau_{nn}^{CE} \tag{46}$$

$$F_{t1-mom} = \rho u_n u_{t1} - \tau_{nt1}^{CE} \tag{47}$$

$$F_{tr-energy} = \rho u_n\left(\frac{3}{2}RT + \frac{u^2}{2}\right) + pu_n - \left(\tau_{nn}^{CE}u_n + \tau_{nt1}^{CE}u_{t1} + \tau_{nt2}^{CE}u_{t2}\right) + q_n^{CE} \tag{48}$$

$$F_{int-energy} = (\Delta q_{Eucken} + \rho u_n e_{int}) = \frac{1}{2}\left(\frac{5-3\gamma}{\gamma-1}\right)pu_n. \tag{49}$$

These correspond to all the expressions in (12) for the orthogonal coordinated system used. Equation (49) provides both the extra term required by (17) as well as the extra term required by (18). However, this returns us to the logical difficulty raised in the discussion following (36) and (37). If the Eucken approximation is introduced when first using (36), then its effect will appear twice when summing (48) and (49), i.e., in the combination $(q_n^{CE} + \Delta q_{Eucken})$. Knowing this, one approach would be to introduce the Eucken approximation here by absorbing Δq_{Eucken} into the term q_n^{CE} by using Eq. (34). Although it appears to be a reasonable step, it is in fact a bold step, because split fluxes are required in (42) and (43) and one cannot be sure that when the Eucken approximation is introduced into χ_2 and

χ_3 in (42) that it will properly account for the absorption of the split quantities $\Delta q^{\pm}_{Eucken}$ in (43). Consequently, one may encounter incorrect energy split fluxes at an interface or a boundary. Actually, we have no alternative, as we do not have $f(C_i, \epsilon)$ with which to compute these split quantities. In the following development, we will use the Eucken approximation throughout and assume that proper accounting is made for $\Delta q^{\pm}_{Eucken}$ by χ_2 and χ_3.

An additional assumption is actually needed to complete the specification of (43), and this involves the evaluation of $e^{\pm}_{int}$, which again requires knowledge of $f(C_i, \epsilon)$. Assuming the Eucken model properly accounts for the correlation $\Delta q_{Eucken} = n < C_n \epsilon >$ then it may be permissible to employ the equilibrium assumption to approximate $e^{\pm}_{int}$. The assumption that the internal energy modes are in equilibrium, both internally and with the translational degrees of freedom, leads to the conclusion that C_i and ϵ are statistically independent random variables, and therefore, $f(C_i, \epsilon)$ reduces to a product function. On this basis $e^{\pm}_{int}$ can be evaluated, and this step leads to the expression following the second equality in (43). However, we should note that if the same assumption were used to evaluate $< C_n \epsilon >$ as well, then we would have $\Delta q_{Eucken} = n < C_n \epsilon >= n < C_n >< \epsilon >= 0$ because $< C_n >= 0$ by definition; and this would lead to the loss of the Eucken approximation. In summary, on combining (42) and (43), our approach consists of absorbing $\Delta q^{\pm}_{Eucken}$ into χ_2 and χ_3 by the introduction of the Eucken approximation and using the equilibrium assumption to evaluate $e^{\pm}_{int}$; this leads to the second expression in (43) as well as the second expression in (49).

A second check leads to the requirement that one should recover the known values for the Maxwellian distribution when setting the nonequilibrium parameters $\hat{\tau}^{CE}$ and $\hat{q}^{CE}$ to zero.

$$F^{\pm}_{zero} = \frac{1}{2}(1 \pm \alpha_1) \tag{50}$$

$$F^{\pm}_{mass} = \rho\sqrt{RT/2}\,[(1 \pm \alpha_1)S_n \pm \alpha_2] \tag{51}$$

$$F^{\pm}_{n-mom} = p\left[(1 \pm \alpha_1)\left(S_n^2 + \frac{1}{2}\right) \pm \alpha_2 S_n\right] \tag{52}$$

$$F^{\pm}_{t1-mom} = \sqrt{2RT}\,[S_{t1} F^{\pm}_{mass}] \tag{53}$$

$$F^{\pm}_{tr-energy} = p\sqrt{RT/2}\left[(1 \pm \alpha_1)S_n(\frac{5}{2} + S^2) \pm \alpha_2\,(2 + S^2)\right] \tag{54}$$

$$F^{\pm}_{int-energy} = \frac{1}{2}\left(\frac{5 - 3\gamma}{\gamma - 1}\right)[RT F^{\pm}_{mass}]\,. \tag{55}$$

These expressions are in full agreement with results obtained by Patterson (Ref. [13], Section 5.3, equations (4), (11), (17) and (19)) where his objective was to compute the momentum and energy exchange at a surface for an equilibrium gas. These relations were later introduced in work by Pullin [15] (for one-dimensional flow) and more recently by Mandal & Deshpande [12] and by Mallett et al. [11].

Finally, on setting the fluid velocities to zero ($S = 0, \alpha_1 = 0, \alpha_2 = 1/\sqrt{\pi}$), one must recover the well-known kinetic theory values for a stationary equilibrium distribution (Maxwellian)

$$F^{\pm}_{zero} = 1/2 \tag{56}$$

$$F^{\pm}_{mass} = \pm\rho\sqrt{RT/2\pi} \tag{57}$$

$$F^{\pm}_{n-mom} = p/2 \tag{58}$$

$$F^{\pm}_{t1-mom} = 0 \tag{59}$$

$$F^{\pm}_{tr-energy} = \pm p\sqrt{2RT/\pi} \tag{60}$$

$$F^{\pm}_{int-energy} = \pm\frac{1}{2}\left(\frac{5-3\gamma}{\gamma-1}\right)p\sqrt{RT/2\pi}. \tag{61}$$

The first five relations clearly agree with known values in kinetic theory, while the final relation is based on several critical assumptions as discussed above.

The importance of the nonequilibrium parameters $\hat{\tau}^{CE}_{ik}$ and $\hat{q}^{CE}_{k}$ in Eqs. (39)-(44) can be judged by comparison with equivalent Euler split fluxes. Of interest in a comparison are the Steger-Warming split fluxes [17] and the equilibrium values given by (51)-(55). Obviously, the nonequilibrium parameters are not constants in a flow, but in a graphical display representative values are quite useful, and a representative peak value for both parameters in a moderately strong normal shock wave is roughly -0.3. This value along with $\gamma = 1.4$ and the assumption of a one-dimensional flow were used to develop Fig. 3, which presents the momentum and energy split fluxes versus the local Mach number for three cases: KFVS for the NS equations given by (40) and (44); KFVS for the Euler equations given by (52) and the sum of (54) and (55); and Steger-Warming splitting. On the scale shown, the results for the equilibrium values and Steger-Warming group fairly closely together (a comparison apparently first made by Mandal and Deshpande [12]), while the present work shows considerable difference, especially in the asymmetrical shift seen in F^+ and F^-. The figure clearly point to the fact that in a hybrid solution, where the one-sided fluxes are to be matched at an interface having nonequilibrium conditions, the present kinetic split fluxes must be used. This is because one does not otherwise know how to adjust the Euler split fluxes, to account for viscous and heat conduction effects, even though the total fluxes are known from (12).

V. BOUNDARY CONDITIONS

When a nonreacting particle in the DSMC method passes through a body surface during a time step, the procedure is to emit the same particle from the surface with a new velocity depending on the boundary conditions. Thus, the DSMC method effectively treats a solid boundary as though it too consists of a gas, but at different conditions. This concept was clearly described by Patterson (Ref. [13], p. 165) and used in his analysis of molecular interactions with boundaries. Because the same particle is emitted, the wall gas is identically the same gas, and therefore the two share the same molecular mass and gas constant. Also, because every particle passing through a body surface is treated this way, the number of particles per unit time per unit area passing into a wall is exactly balanced by the rate of emission. However, this condition does not tell us what the number density of the wall gas is, i.e., it does not fix n_w, or ρ_w, for the wall gas, nor does it fix the temperature of the wall gas T_w. What we do know is that the total mass flux must be zero at a material surface, i.e.

$$(F_{mass})_{surface} = (F^+_{mass})_g + (F^-_{mass})_w = 0, \tag{62}$$

where gas and wall positions, consistent with the end-wall geometry shown in Fig. 2, are assumed. Generally speaking, in the DSMC method one often assumes that the wall gas is in equilibrium and the wall is stationary. On this basis, Eq. (57) can be used in (62) to describe the wall gas, and we can write

$$(F^+_{mass})_g = \rho_w\sqrt{RT_w/2\pi}. \tag{63}$$

A particularly simple boundary condition is the case where the wall temperature T_w is specified, namely, an isothermal boundary condition; and for this case, Eq. (63) fixes the density of the wall gas ρ_w, since $(F^+_{mass})_g$ would be known from (39) and the state of the gas from the update procedure for the numerical solution of the NS equations. Given ρ_w, T_w and $p_w = \rho_w RT_w$, we then have on using (58) the relation

$$(F_{n-mom})_{surface} = (F^+_{n-mom})_g + p_w/2, \tag{64}$$

which fixes the normal stress at the surface, since $(F^+_{n-mom})_g$ likewise represents a known quantity from (40) and the update procedure. Likewise, on using (59), we have

$$(F_{t1-mom})_{surface} = (F^+_{t1-mom})_g, \tag{65}$$

which determines the tangential stress on the surface. Finally, the energy flux to the surfaces is found by using (60) and (61) together with (44) and the state of the gas from the update procedure, i.e.

$$(F_{energy})_{surface} = (F^+_{energy})_g - p_w\sqrt{2RT_w/\pi}\left[1+\frac{1}{4}\left(\frac{5-3\gamma}{\gamma-1}\right)\right], \tag{66}$$

which completes the specification of the conditions at a surface for an isothermal wall. The most important outcome from this analysis is that the temperature of the gas near the surface may not be equal to the specified wall temperature T_w, which gives rise to the possibility of temperature slip. Likewise, the tangential velocity near the surface may not be zero, leading to velocity slip; however, the normal velocity near the surface must be zero because the expressions in (62) also define the fluid velocities for the two separate gases.

For an adiabatic boundary condition, we know that the total energy flux to the surface is zero, while the wall gas temperature and density are unknown. Thus, we have

$$(F_{energy})_{surface} = (F^+_{energy})_g + (F^-_{energy})_w = 0, \tag{67}$$

and on using (60) and (61) for the wall gas, we have

$$(F^+_{energy})_g = p_w \sqrt{2RT_w/\pi} \left[1 + \frac{1}{4}\left(\frac{5-3\gamma}{\gamma-1}\right)\right], \tag{68}$$

which along with (63) provides two equations in the two unknowns ρ_w and T_w, since $(F^+_{mass})_g$ and $(F^+_{energy})_g$ are both known from the update procedure at each time step. Likewise, the normal stress on the surface can be obtained using (58) and the tangential stress using (59), completing the analysis.

The application of flux boundary conditions to the wide variety of possible boundary conditions is quite straightforward and only two are given here. For example, accommodation coefficients for momentum and energy are often used in the application of the DSMC method, and it would be a simple matter to include them as well. In addition, analytical results for both temperature slip and velocity slip can be obtained from Eqs. (62)-(68) and these can be shown to reproduce the special case considered by Patterson (Ref. [13], Section 4.4, equations (30)-(33)). A detailed discussion of this topic will be covered in a follow-on report.

VI. NUMERICAL COMPARISONS

Our main objective is to show that the derived expressions for the split kinetic fluxes given by Eqs. (39)-(44), together with the flux boundary conditions, lead to valid solutions of the NS equations. For this purpose, comparisons are made with first-order schemes by Steger & Warming [17] and Roe [16] , while second-order comparisons are made with the symmetric limited positive second-order (SLIP2) scheme reported by Tatsumi, Martinelli & Jameson [18]. Central differencing was used in each of these cases to handle the terms introduced by viscous stress and heat flux. A version of the monotone upstream-centered scheme for conservation laws (MUSCL), van Leer [19], was used in applying the KFVS relations for the NS equations. The parameters chosen in using MUSCL are defined in the following relations

$$F^{MUSCL}_{i+\frac{1}{2}} = F^+_{i+\frac{1}{2}} + F^-_{i+\frac{1}{2}}, \tag{69}$$

where

$$\begin{aligned}
F^+_{i+\frac{1}{2}} &= F^+(U^L_{i+\frac{1}{2}}) \\
F^-_{i+\frac{1}{2}} &= F^-(U^R_{i+\frac{1}{2}}) \\
U^L_{i+\frac{1}{2}} &= U_i + \frac{\theta_1}{2} minmod\left[\Delta U_{i-\frac{1}{2}}, \beta \Delta U_{i+\frac{1}{2}}\right] \\
U^R_{i+\frac{1}{2}} &= U_{i+1} - \frac{\theta_1}{2} minmod\left[\Delta U_{i+\frac{3}{2}}, \beta \Delta U_{i+\frac{1}{2}}\right] \\
\Delta U_{i+\frac{1}{2}} &= U_{i+1} - U_i \\
minmod(a,b) &\equiv \begin{cases} a & if \quad |a| \le |b| \quad \& \quad ab > 0 \\ b & if \quad |a| > |b| \quad \& \quad ab > 0 \\ 0 & if \quad\quad\quad\quad\quad ab < 0 \end{cases}
\end{aligned}$$

and where the L/R arrangement is defined in Fig. 4. A first-order scheme is obtained for $\theta_1 = 0$ and a second-order scheme for $\theta_1 = 1$. Most of the work was carried out for $\beta = 1.5$. The function $F^+(U^L)$, for example, represents any one of the equations (39), (40), (41) or (44). These equations contain spatial derivatives of U as well, and the concept of the function must be generalized to include them. For a problem with one spatial dimension, the update formula (first-order in time) is then given by

$$U^{n+1}_i = U^n_i - \frac{\Delta t}{\Delta x}\left(F^{MUSCL}_{i+\frac{1}{2}} - F^{MUSCL}_{i-\frac{1}{2}}\right)^n, \tag{70}$$

where n represents the time step.

The problem of determining the profile for a normal shock wave represents a steady flow for which viscous stress and heat conduction are very important; and this represents an extreme limit that provides appropriate conditions for testing. Although it is well known that the NS equations do not give physically realistic profile predictions for strong shock waves, we are only interested in establishing that valid NS solutions are being obtained. For this purpose, we have the method suggested by von Mises [21] and by Gilbarg & Paolucci [7] for solving the NS equations for steady one-dimensional flow, which can be used as a standard of comparison. To obtain a reliable reference, a four-step Runge-Kutta method and 1200 points in the domain of integration were used. The primary integration takes place in a computational space where the fluid velocity is the independent variable and, because the normal stress and the heat flux variables seem to show the greatest numerical sensitivity, these were selected for display. Figures 5 and 6 give results for a shock-wave Mach number of 1.5 and air as a representative gas. First-order schemes for KFVS, Steger-Warming and Roe are compared with the reference solution (solid curve) in Fig. 5; and it is clear that Roe's scheme compares the best, with Steger-Warming exhibiting the familiar transition near the sonic station and KFVS showing only moderate success. Second-order schemes consisting of KFVS and Jameson's SLIP2, along with the reference solution, are compared in Fig. 6; and it is clear that it is not possible to distinguish between them. Higher Mach numbers were also studied and the same general observations were made.

In the same spirit of reviewing extreme conditions, it is appropriate to consider a flow that corresponds to the Euler limit, namely, a shock-tube flow. Because of the presence of the contact surface, it is most useful to display the density and temperature variables as they frequently exhibit large changes there. Figs. 7 and 8 present results for pressure ratios (driver to driven gas) of 3 and 20, respectively, and where the flow is from left to right. Starting from the left, the transitions seen are the expansion fan, the contact surface, and the shock wave. We see that there is good agreement between second-order KFVS and SLIP2, with the largest difference at the contact surface, possibly a result of the different limiters used. Roe's first-order scheme clearly shows severe rounding of the profiles. The separation distance between the shock wave and the contact surface grows linearly with time and therefore the relative rounding of the corners would appear to diminish with increasing time. An early time was specifically chosen for display to emphasize the relative difference between the different schemes.

In both the ideal shock-tube and shock-wave problems solid boundaries are absent. However, the case of an impulsively started piston is an example where nonequilibrium effects near a solid boundary can lead to temperature slip. Figure 9 shows an expanded view of the thermal layer near an isothermal piston, where the piston Mach number is taken to be unity and the gas is ideal and monatomic, and it is clear that the gas temperature near the piston is higher than the piston temperature, as a result of the flux type (DSMC) boundary conditions used in solving the problem. A theoretical expression for temperature slip in a slightly rarefied flow of a monatomic gas was developed by Patterson [13] (see equation (33), p. 125) and his prediction is shown by the circle symbol. The excellent agreement seen undoubtedly results from the fact that Petterson's theory makes use of the assumptions in NS, and therefore, boundary conditions (62)-(68) used in the numerical solution and the analytical approach used by Patterson correspond closely. A necessary next step, of course, is to carry out comparisons with DSMC simulations to determine the conditions under which the magnitude of the jump is physically correct. This study, which requires careful discussion, will be presented in a follow-on report. The most important observation is that the method introduces slip into the NS formulation in a very natural way through the use of flux boundary conditions.

A final problem to be reviewed is the steady, two-dimensional flow produced by a plate sliding across the open end of a square cavity, and for which the temperatures of all four material surfaces are held fixed and equal. This is a well-known problem for which the NS solution, based on the no-slip boundary condition, leads to singular behavior of the shearing stress, in the two corners defined by the slider plate and the box walls [1]. Because of the shearing motion of the plate, work is done on the fluid, it induces a circulation inside the box, and the fluid is heated as a result of viscous dissipation. However, because of the isothermal walls, heat is conducted out of the gas, and a steady state is reached after a long time has passed. The velocity field shown in Fig. 10 provides an intuitive physical understanding of the flow generated by the sliding plate, which is on top and moves from right to left in the view shown. The computational domain was covered by 64×64 square cells, the plate Mach number was set to 1.0, the Knudsen number (based on the cavity dimension) was set at 0.005, and the gas was assumed to be air at ambient conditions. One of the more interesting results from the solution is the temperature distribution in the box, which is shown in Fig. 11. The dimensionless wall temperature is unity in the figure. If no-slip were present, then the dimensionless gas temperature would also be unity everywhere along the surface, but it can be seen that a significant jump occurs around a great portion of the cavity walls. The same situation develops for the two components of velocity. Figure 12 displays the velocity component parallel to the slider plate (near face) which is moving left to right in the view shown. If no-slip were present, then the dimensionless gas velocity would be unity (negative) over the length of the plate and zero everywhere else on the box boundary. As can be seen, a significant jump in velocity occurs over the entire plate and, as a result, it appears to suppress the singular behavior of the stress in the two corners. Although the edge-values displayed are actually the values at the midpoints of the cells bordering the walls and one

must find the true wall values from extrapolation, the correction is modest and our observations remain unchanged. The small ripples seen in the Fig. 12 are believed to be small vortices that are not fully resolved by the grid used.

VII. CONCLUDING REMARKS

Our work has been guided by the interest in developing a hybrid method using DSMC and NS, where the focus here was limited to a method for handling the NS portion. An Euler scheme introduced by Pullin [15] and further developed by Mandal & Deshpande [12] and by Mallett et al. [11], was generalized through use of kinetic-theory concepts to cover the NS equations, and second-order solutions were shown to compare well with established second-order numerical schemes for the NS equations. Because matching must take place in the near-continuum regime, where both DSMC and NS are valid, the NS portion must account for slip at solid boundaries. Use of the kinetic split fluxes was shown to lead to a very natural implementation of DSMC type boundary conditions, and these led to the appearance of slip. Likewise, use of the kinetic split fluxes at an interface between DSMC and NS in a hybrid solution is also expected to be necessary in order to model the correct physics in a nonequilibrium flow, especially when determining the inputs to the DSMC portion. In view of this, the equation set (39)-(44), representing KFVS for the NS equations, is clearly needed in interfacing with DSMC and in applying boundary conditions at a solid surface for the NS portion of a hybrid solution. However, the added step of also using a KFVS scheme for the NS solution itself is not an absolute requirement, as one could argue that any numerical solution of the NS equations would be acceptable, as long as these kinetic split fluxes were used in applying all boundary conditions. Because the DSMC portion is normally expected to take the greater computation time in most problems, one does not need to pick a numerical scheme for the NS portion that minimizes time, and therefore, computation time is not an issue. This allows one to choose a numerical scheme that offers the greatest compatibility with DSMC, which we believe to be the KFVS scheme for the NS equations. On the other hand, in obtaining the data for Figs. 7 and 8, it was found that KFVS and Jameson's SLIP2 required virtually the same computation time. Whether this continues to hold for higher spatial dimensions is unknown.

VIII. ACKNOWLEDGMENTS

Many helpful discussions with Tawei Lou and Douglas C. Dahlby concerning their recent DSMC results are gratefully acknowledged. This work was supported in part by NASA under Grant NCC2-5072.

---

[1] G. K. Batchelor, *An Introduction to Fluid Dynamics* (Cambridge Univ. Press, Cambridge, 1967).
[2] G. A. Bird, *Annu. Rev. Fluid Mech.* **10**, 11 (1978).
[3] G. A. Bird, *Molecular Gas Dynamics and the Direct Simulation of Gas Flows* (Clarendon Press, Oxford, 1994).
[4] J. E. Broadwell, *J. Fluid Mech.* **19**, 401 (1964).
[5] S. Chapman and T. G. Cowling, *The Mathematical Theory of Non-Uniform Gases* (Cambridge Univ. Press, Cambridge, 1960).
[6] S. Y. Chou, Ph. D. thesis, Stanford University, 1995.
[7] D. Gilbarg and D. Paolucci, *J. Rat. Mech. and Anal.* **2**, 617 (1953).
[8] C. F. Gooch, Ph. D. thesis, Stanford University, 1993.
[9] H. Grad, *Commun. Pure Appl. Math.* **2**, 331 (1949).
[10] M. N. Macrossan and R. I. Oliver, *Int. J. Num. Meth. Fl.* **17**, 177 (1993).
[11] E. R. Mallett, D. I. Pullin, and M. N. Macrossan, *AIAA J.* **33**, No. 9, 1626 (1995).
[12] J. C. Mandal and S. M. Deshpande, *Comput. & Fluids* **23**, 447 (1994).
[13] G. N. Patterson, *Molecular Flow of Gases* (John Wiley, New York, 1956).
[14] K. H. Prendergast and K. Xu, *J. Comput. Phys.* **109**, 53 (1993).
[15] D. I. Pullin, *J. Comput. Phys.* **34**, 231 (1980).
[16] P. L. Roe, *Annu. Rev. Fluid Mech.* **18**, 337 (1986).
[17] J. L. Steger and R. F. Warming, *J. Comput. Phys.* **40**, 263 (1981).
[18] S. Tatsumi, L. Martinelli, and A. Jameson, *AIAA J.* **33**, No. 2 (1995).
[19] B. van Leer, *J. Comput. Phys.* **32**, 101 (1979).

[20] W. G. Vincenti and C. H. Kruger, Jr., *Introduction to Physical Gas Dynamics* (John Wiley, New York, 1965).
[21] R. von Mises, *J. Aero. Sci.* **17**, 551 (1950).
[22] L. C. Woods, *An Introduction to the Kinetic Theory of Gases and Magnetoplasmas* (Oxford Univ. Press, Oxford, 1993).

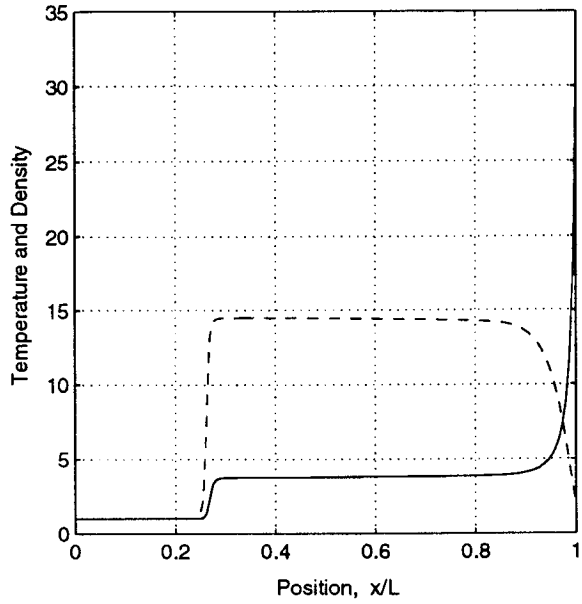

FIG. 1. Temperature (T/T1, - - -) and density ($\rho/\rho 1$, ——) ahead of an impulsively started piston in a stationary gas (state 1), where piston Mach number = 5.0, $\gamma = 5/3$ and piston temperature is held fixed. The piston is located at $x/L = 1$.

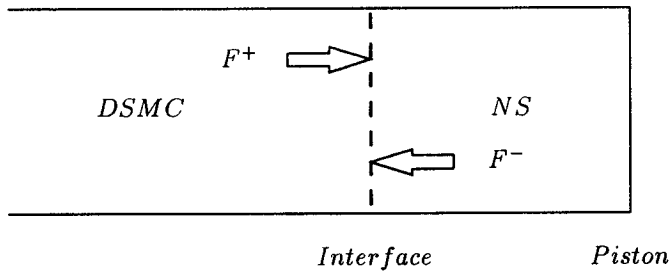

FIG. 2. A schematic representation of a hybrid scheme joining the direct simulation Monte Carlo (DSMC) method and a Navier-Stokes (NS) numerical method.

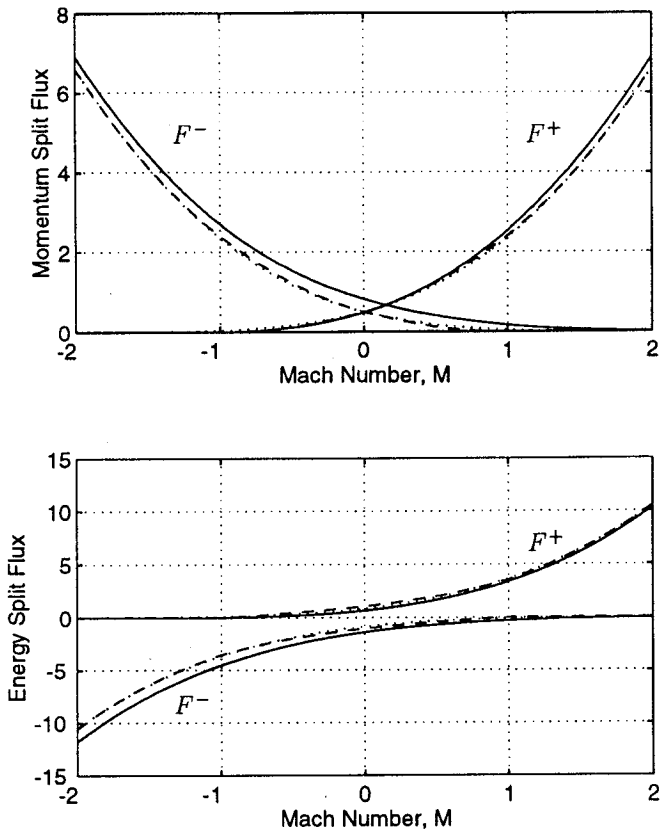

FIG. 3. Momentum and energy split fluxes for the case of a one-dimensional flow and $\gamma = 1.4$. The momentum flux is nondimensionlized by p and the energy flux by $p(2RT)^{1/2}$. Comparisons are for the present work, where the assumption $\hat{\tau}_{nn}^{CE} \approx \hat{q}_n^{CE} \approx -0.3$ was made in Eqs. (40) and (44), —— ; Mandal-Deshpande KFVS for the Euler equations, $\cdots$; and Steger-Warming, - - - - .

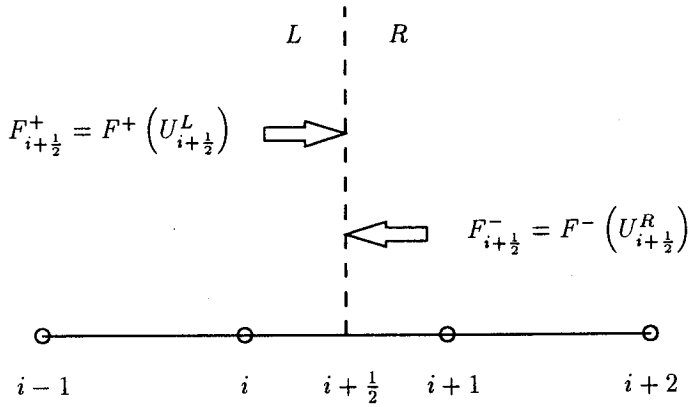

FIG. 4. Definition of symbols used in applying the MUSCL scheme to the KFVS relations for the NS equations.

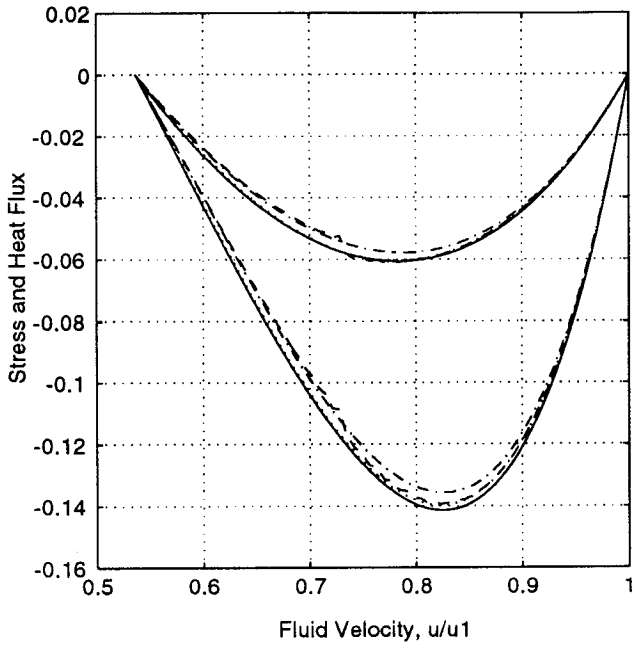

FIG. 5. Normal stress (upper set, $\tau_{nn}/2p$) and heat flux (lower set, q_n/pc) in a shock wave versus the fluid velocity, with the upstream state designated by 1, $M_1 = 1.5$, and $\gamma = 1.4$. The curves were separated by using a factor of 2 in plotting the dimensionless stress. First-order schemes for KFVS, - · - ·, Steger-Warming, - - -, and Roe, ····, are compared with the reference solution, ——.

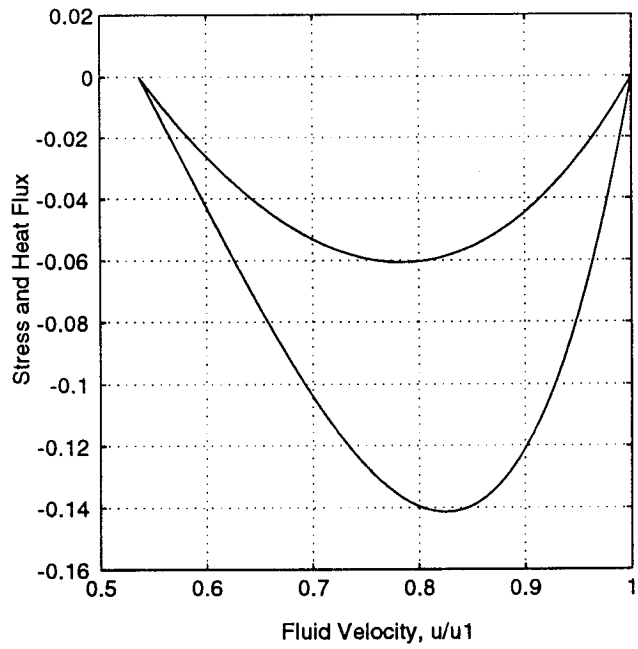

FIG. 6. Normal stress (upper set, $\tau_{nn}/2p$) and heat flux (lower set, q_n/pc) in a shock wave versus the fluid velocity, with the upstream state designated by 1, $M_1 = 1.5$, and $\gamma = 1.4$. The curves were separated by using a factor of 2 in plotting the dimensionless stress. Second-order schemes for KFVS, - · - ·, and Jameson's SLIP2, - - -, are compared with the reference solution, ——.

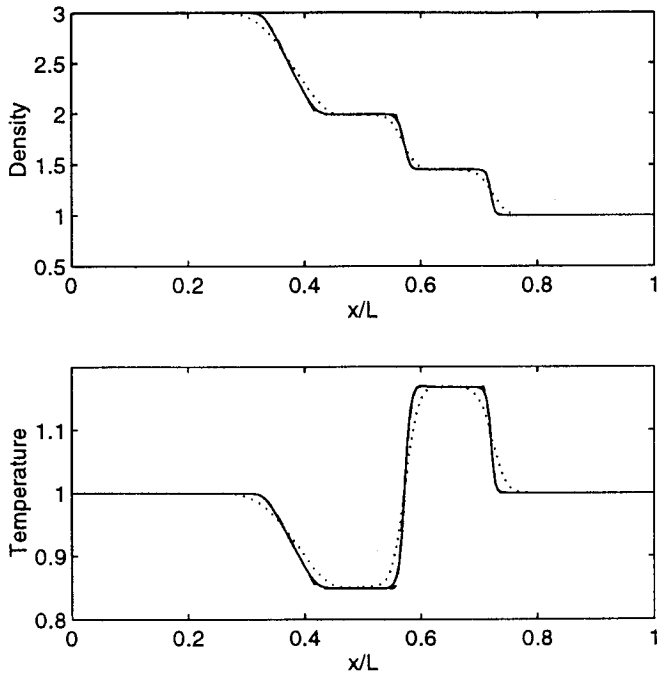

FIG. 7. Shock-tube flow for a pressure ratio of 3, $\gamma = 1.4$, and where the flow is from left to right. Comparisons are for second-order KFVS, ——, Jameson's SLIP2, - - -, and first-order Roe, · · · ·. The variables shown are the density $\rho/\rho 1$ and the temperature $T/T1$, where state 1 refers to upstream conditions.

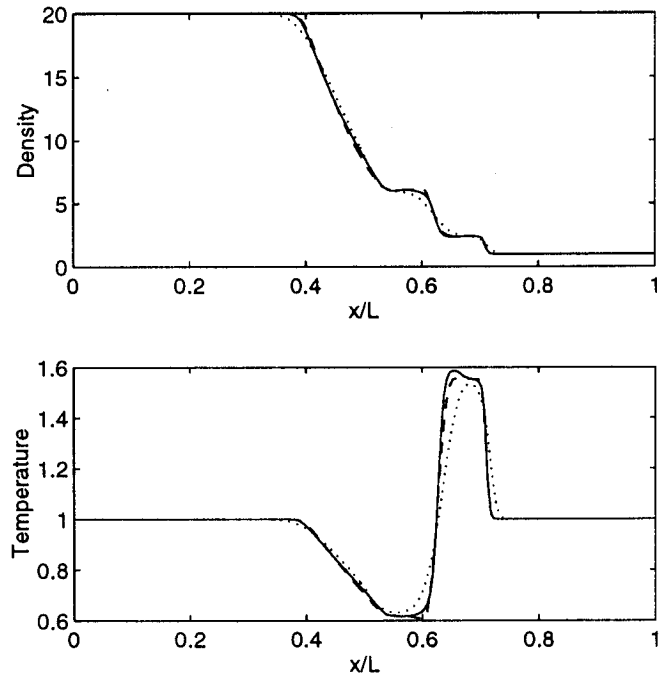

FIG. 8. Shock-tube flow for a pressure ratio of 20, $\gamma = 1.4$, and where the flow is from left to right. Comparisons are for second-order KFVS, ——, Jameson's SLIP2, - - -, and first-order Roe, · · · ·. The variables shown are the density $\rho/\rho 1$ and the temperature $T/T1$, where state 1 refers to upstream conditions.

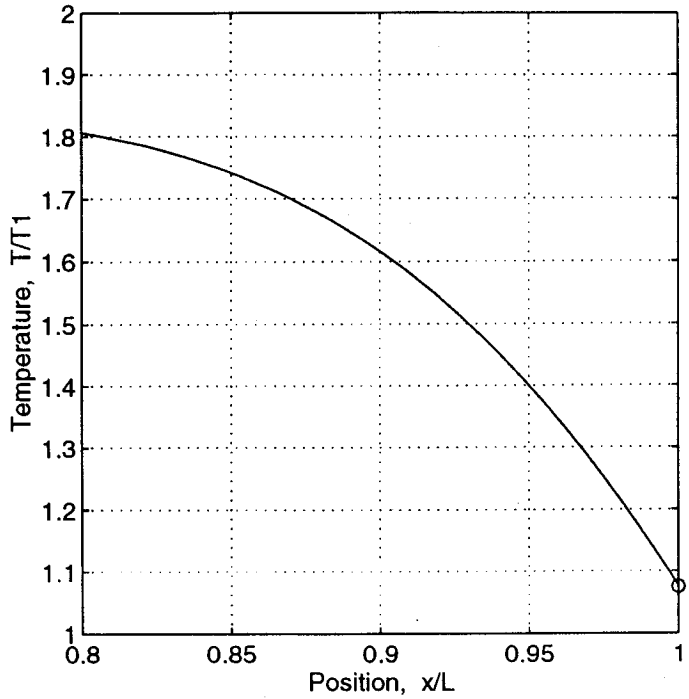

FIG. 9. Temperature ahead of an impulsively started piston in a stationary monatomic gas, where piston Mach number = 1.0 and where use of the flux boundary condition for an isothermal piston leads to a temperature slip at the piston surface (located at $x/L = 1$). Also shown, by the circle symbol, is Patterson's theory [11] for temperature slip in a slightly rarefied monatomic gas.

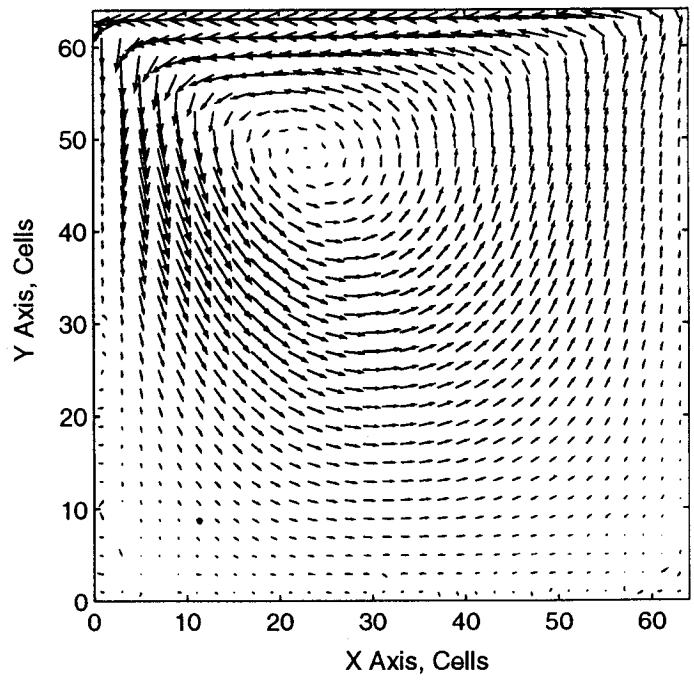

FIG. 10. Velocity field in a square isothermal cavity with a slider plate on top, moving from right to left at a Mach number of 1.0. The gas is assumed to be air and Kn (based on the cavity width) = 0.005.

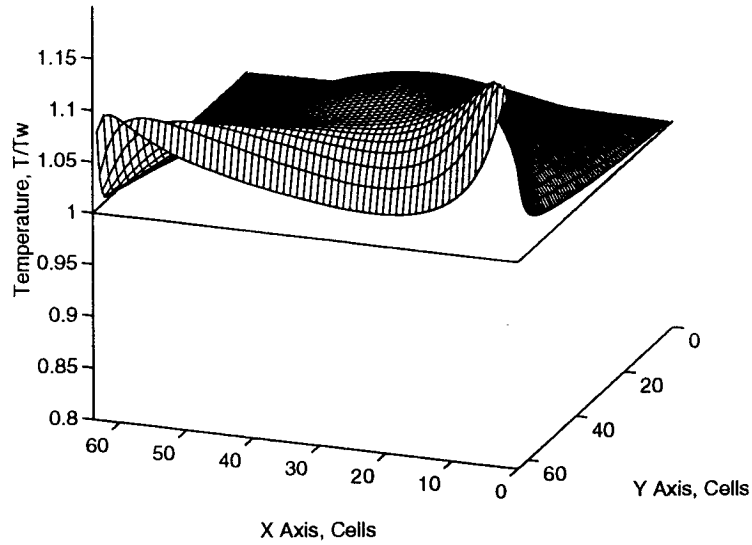

FIG. 11. Temperature distribution in a square isothermal cavity with a slider plate (near face) moving from left to right in view shown; conditions same as in Fig. 10.

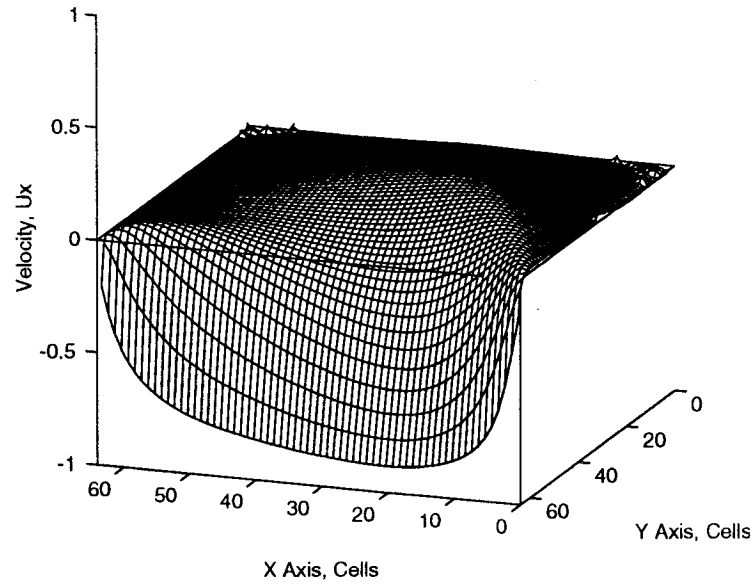

FIG. 12. Velocity component parallel to the slider plate (near face) which is moving from left to right in view shown; conditions same as in Fig. 10 with velocity scaled to the sound speed at the wall temperature.

APPENDIX B

A Numerical Study Comparing Kinetic Flux-Vector Splitting for the Navier-Stokes Equations with a Particle Method

T. Lou, D. Dahlby and D. Baganoff
Department of Aeronautics and Astronautics
Stanford University, Stanford, CA 94305
(Submitted to: Journal of Computational Physics, April 30, 1996)

Numerical solutions based on the method of kinetic flux-vector splitting (KFVS) for the Navier-Stokes equations are compared with the direct simulation Monte Carlo method (DSMC) for three problems: an impulsively started piston, which emphasizes heat flux; an impulsively started flat plate, which emphasizes shearing stress; and a plate sliding past a square cavity, or the lid-driven cavity problem, which combines both stress and heat flux. Taking the view that the DSMC method provides the correct physical description near material boundaries, the comparisons, which were carried out for the conditions of a slightly rarefied flow, show good agreement for temperature and velocity slip, and in the prediction of the kinetic split fluxes, verifying the assumptions and the approach taken in the KFVS method.

I. INTRODUCTION

The theoretical development for the method of kinetic flux-vector splitting (KFVS) for the Navier-Stokes equations was introduced in Ref. [4], which represents an extension of work initiated by Deshpande for the Euler equations [6,7]. Additionally, it was shown to give good agreement with established numerical schemes for the Navier-Stokes equations. Boundary conditions based on the new split fluxes and the kinetic theory were also developed and shown to predict slip at a material surface, as a gas becomes rarefied. However, confirmation for the magnitude of the predicted slip and the conditions under which the correct predictions are found were not fully explored. Also not given was support for the use of a critical approximation, based on the Eucken model, which was introduced to carry out the flux-splitting for energy, in the case of a gas having internal structure. The objective of the present work is to provide the appropriate analysis by comparing the predictions of the theory presented in [4] with the results of simulations carried out with the direct simulation Monte Carlo (DSMC) method [2,3], a method of simulation where a large collection of particles is used to model a rarefied gas flow. Of course, the comparisons can only be carried out in the near-continuum regime where the computational cost for the DSMC method does not become prohibitive. Likewise, for the NS equations to hold, the flow can only be slightly rarefied and the magnitudes of stress and heat flux must lie in a range where the occurrence of slip near a solid surface represents the principal modification to the fluid physics. However, these conditions are wholly consistent with the objective in [4], where the KFVS method was introduced as the continuum counterpart to the DSMC method in an eventual construction of a hybrid scheme combining the two.

The version of the DSMC method used in this study [1,8] divides space into uniform cubical cells. These cells are used to identify which particle pairs are candidates for collision during a time step and to compute cell-averaged macroscopic quantities at the end of a time step. In general terms, the DSMC method is expected to give reliable results when the local mean free path length is large compared with the cell dimension. Particular experience with the case of Couette flow has shown that good agreement for viscous stress and heat flux is obtained between DSMC and NS when the cell Knudsen number is greater than unity, and progressively more modest agreement is found as it is made smaller [5]. In our comparisons, the local cell Knudsen number appearing in the DSMC simulations was set at unity or greater for the most dense parts of each flow. The molecular model chosen for the simulations was the hard-sphere molecule, for which the transport coefficients vary as the square root of the temperature. In the case of a diatomic gas, the vibrational mode was not excited, while the rotational degrees of freedom were set to be in equilibrium with the translational degrees of freedom, by setting the so-called collision number to unity. In the DSMC simulation, this leads to the ideal diatomic gas for which $\gamma = 7/5$.

Two issues are addressed in this study: (i) in the case of a simple gas, the theory in [4] is rather securely founded, and therefore, the primary question relates to whether the magnitude of the predicted slip, for the particular flow conditions considered, is in agreement with results obtained from DSMC simulations; and (ii) in the case of a gas with internal structure, the flux splitting employed in [4] is based on the Eucken approximation, which directly affects the predicted split energy fluxes, and the particular approximation used requires confirmation, especially at an isothermal material surface where nonequilibrium effects may be quite large. These questions will be investigated by studying the highly nonequilibrium flow produced near material surfaces for three problems: an impulsively started piston,

which emphasizes heat flux; an impulsively started flat plate, which emphasizes shearing stress; and a plate sliding past a square cavity, or the lid-driven cavity problem, which combines both stress and heat flux.

II. THE KFVS EQUATIONS

The split kinetic fluxes for the Navier-Stokes equations are given by equations (39)-(44) in Ref. [4] and these are reproduced for use here, where the notation employed is the same, and they read:

$$F^{\pm}_{mass} = \rho\sqrt{RT/2}\left[(1 \pm \alpha_1)S_n \pm \alpha_2\,(1 - \chi_1)\right] \tag{1}$$

$$F^{\pm}_{n-mom} = p\left[(1 \pm \alpha_1)\left(S_n^2 + \frac{1}{2}(1 - \hat{\tau}^{CE}_{nn})\right) \pm \alpha_2\left(S_n + \hat{q}^{CE}_n\right)\right] \tag{2}$$

$$F^{\pm}_{t1-mom} = \sqrt{2RT}\left[S_{t1}F^{\pm}_{mass}\right] + \frac{1}{2}p\left[-(1 \pm \alpha_1)\hat{\tau}^{CE}_{nt1} \pm \alpha_2\hat{q}^{CE}_{t1}\right] \tag{3}$$

$$F^{\pm}_{tr-energy} = p\sqrt{RT/2}\left[(1 \pm \alpha_1)\left(S_n(\frac{5}{2} + S^2) + \chi_2\right) \pm \alpha_2\,(2 + S^2 + \chi_3)\right] \tag{4}$$

$$F^{\pm}_{int-energy} = (\Delta q^{\pm}_{Eucken} + \rho u_n e^{\pm}_{int}) = \frac{1}{2}\left(\frac{5 - 3\gamma}{\gamma - 1}\right)\left[RTF^{\pm}_{mass}\right] \tag{5}$$

$$F^{\pm}_{energy} = F^{\pm}_{tr-energy} + F^{\pm}_{int-energy}, \tag{6}$$

where

$$\begin{aligned}
&\alpha_1 = erf(S_n), \qquad \alpha_2 = \frac{1}{\sqrt{\pi}}e^{-S_n^2}\\
&\chi_1 = \left[S_n\hat{q}^{CE}_n + \frac{1}{2}\hat{\tau}^{CE}_{nn}\right]\\
&\chi_2 = \left[\frac{5}{2}\hat{q}^{CE}_n - \left(S_n\hat{\tau}^{CE}_{nn} + S_{t1}\hat{\tau}^{CE}_{nt1} + S_{t2}\hat{\tau}^{CE}_{nt2}\right)\right]\\
&\chi_3 = \left[S_{t1}\hat{q}^{CE}_{t1} + S_{t2}\hat{q}^{CE}_{t2} - \chi_1\left(1 + S_{t1}^2 + S_{t2}^2\right) - \hat{\tau}^{CE}_{nn}\right]\\
&S_n = u_n/\sqrt{2RT}, \qquad S^2 = S_n^2 + S_{t1}^2 + S_{t2}^2\\
&\hat{\tau}^{CE}_{nn} = \tau^{CE}_{nn}/p, \qquad \hat{q}^{CE}_n = \frac{2}{5}q^{CE}_n/(p\sqrt{2RT})\\
&q^{CE}_i = -K^{(1)}\frac{\partial T}{\partial x_i}\\
&\tau^{CE}_{ij} = \mu^{(1)}\left(\frac{\partial u_i}{\partial x_j} + \frac{\partial u_j}{\partial x_i}\right) - \frac{2}{3}\mu^{(1)}\left(\frac{\partial u_k}{\partial x_k}\right)\delta_{ij}.
\end{aligned}$$

A Cartesian coordinates system is assumed in the above equations, with the normal direction represented by n, and the two tangential directions by $t1$ and $t2$. The dimensionless velocity S (speed ratio) determines the two parameters α_1 and α_2, while the dimensionless, Chapman-Enskog expressions for stress $\hat{\tau}^{CE}_{ij}$ and heat flux $\hat{q}^{CE}_n$ are the nonequilibrium factors in the quantities χ_1, χ_2 and χ_3. The sign convention employed assumes the positive split flux F^+ points in the direction of increasing n, and is directed out of a surface enclosing a body of gas. The convention for F^- is based on the splitting $F = F^+ + F^-$, where F is the total flux, and therefore it often evaluates to a negative value. The corresponding expression for $F^{\pm}_{t2-mom}$ is not listed as it can be inferred from (3).

Extreme nonequilibrium conditions in a gas are found near isothermal boundaries, where the one-sided fluxes are large, and these provide special conditions for detailed study. The relations developed for an isothermal boundary are given by equations (63)-(66) in Ref. [4] and these are also listed below, where again the same notation is followed.

$$(F^{+}_{mass})_g = \rho_w\sqrt{RT_w/2\pi}, \tag{7}$$

$$(F_{n-mom})_{surface} = (F^{+}_{n-mom})_g + p_w/2, \tag{8}$$

$$(F_{t1-mom})_{surface} = (F^{+}_{t1-mom})_g, \tag{9}$$

$$(F_{energy})_{surface} = (F^{+}_{energy})_g - p_w\sqrt{2RT_w/\pi}\left[1 + \frac{1}{4}\left(\frac{5-3\gamma}{\gamma-1}\right)\right]. \tag{10}$$

In the above relations, the state of the gas near a surface is denoted by subscript g, while the state of the hypothetical wall gas is denoted by subscript w. These relations were developed in [4] using DSMC type boundary conditions for a nonreacting gas, in which the wall can be viewed as a hypothetical gas at conditions determined by the particular boundary conditions employed. In this case, the wall gas is the same gas because of the assumed nonreacting interaction between gas molecules. Likewise, the sign convention assumed in the boundary conditions (7)-(10) is one where a positive flux points in the direction of positive n, when viewed from the position of the gas at an interface with a wall.

III. IMPULSIVELY STARTED PISTON

The interest in an impulsively started piston is associated with the fact that the heat transfer rate to an isothermal piston can be very high at early time, leading to large nonequilibrium effects. On the other hand, the impulsive start requires special attention, as will be seen. Because it is not obvious from the structure of Eqs. (7)-(10) how the condition of zero slip is recovered in the continuum limit, and because DSMC simulations become overly costly in this limit, it is desirable to further develop the theoretical expressions so that comparisons can be more readily assessed. The continuum limit is obtained for conditions of high pressure and large time when the boundary layer is relatively thick in relation to the local mean free path length; and for the one-dimensional geometry of an impulsively started piston, where the $t1$ and $t2$ coordinates are ignored, this leads to small values of the surviving dimensionless derivatives $\hat{\tau}^{CE}_{nn}$ and $\hat{q}^{CE}_{n}$, with $\hat{\tau}^{CE}_{nn} \ll \hat{q}^{CE}_{n}$. For calculational purposes, it is easier to consider a moving gas and a stationary piston, and therefore, at the piston surface it is appropriate to set the speed ratio to zero, i.e. $S_n = 0$, and thus, $\alpha_1 = 0$ and $\alpha_2 = 1/\sqrt{\pi}$. On using (1) to represent the gas near a surface and on using boundary condition (7), the following relations between the conditions in the gas flow and the hypothetical wall-gas values are obtained

$$\frac{\rho_g}{\rho_w}\left(1 - \frac{1}{2}\tilde{\tau}^{CE}_{nn}\right) = \sqrt{\frac{T_w}{T_g}}, \qquad \frac{p_g}{p_w}\left(1 - \frac{1}{2}\tilde{\tau}^{CE}_{nn}\right) = \sqrt{\frac{T_g}{T_w}}, \tag{11}$$

where $p = \rho RT$ is used for both the gas flow and the hypothetical wall gas. When Eqs. (4)-(6) are substituted into boundary condition (10) and on making use of (11) we obtain, for the total energy flux at the surface, the relation

$$\frac{4(F_{energy})_{surface}}{p_g\sqrt{2RT_g}} = .5\hat{q}^{CE}_{n} + \frac{1}{\sqrt{\pi}}\left(\frac{\gamma+1}{\gamma-1}\right)\left(1 - \frac{T_w}{T_g}\right) - \frac{1}{2\sqrt{\pi}}\left[\left(\frac{3\gamma-1}{\gamma-1}\right) - \left(\frac{\gamma+1}{\gamma-1}\right)\left(\frac{T_w}{T_g}\right)\right]\hat{\tau}^{CE}_{nn}. \tag{12}$$

The definition for the total energy flux in the coordinate system for which $S_n = 0$ simplifies to the relation $(F_{energy})_{surface} = q^{CE}_{n}$, and consequently, the above equation reduces to

$$\left(1 - \frac{1}{2}\hat{\tau}^{CE}_{nn}\right)\frac{T_w}{T_g} = 1 - 5\sqrt{\pi}\left(\frac{\gamma-1}{\gamma+1}\right)\hat{q}^{CE}_{n} - \frac{1}{2}\left(\frac{3\gamma-1}{\gamma+1}\right)\hat{\tau}^{CE}_{nn}. \tag{13}$$

For an isothermal piston, heat conduction represents the dominant effect at large time, and therefore, the above equation can be approximated, for $\hat{\tau}^{CE}_{nn} \ll 1$, by

$$\frac{T_w}{T_g} = 1 - \left(\frac{\gamma-1}{\gamma+1}\right)\left(5\sqrt{\pi}\hat{q}^{CE}_{n} + \hat{\tau}^{CE}_{nn}\right), \tag{14}$$

which shows that the gas temperature near the surface T_g approaches the wall temperature T_w, as the magnitudes of the nonequilibrium parameters become smaller and smaller in approaching the continuum limit (because of increasing p).

Likewise, for positive heat flux (into the wall) the gas temperature is greater than the wall temperature (temperature slip). An equivalent slip condition, for the case of slightly rarefied flow of a monatomic gas, was obtained by Patterson [9] and it is easy to show that Eq. (14) fully agrees with Patterson's result (cf. equation (33), p. 125). This agreement is found on setting $\gamma = 5/3$, Prandtl number $= 2/3$, and then approximating (14) for the inverted ratio T_g/T_w. Additionally, it has been shown by Shidlovskiy [10], again for the case of a monatomic gas, that inclusion of the thermal accommodation coefficient α introduces a factor $(2-\alpha)/\alpha$ multiplying the heat flux term (cf. equation (3.16), p. 67). Equation (14) was developed here for two purposes: to show that the KFVS formulation (1)-(6) and the associated boundary conditions (7)-(10) agree with related work, and to introduce the extension to the case of a polyatomic gas.

Returning to the more descriptive view, where the gas and piston are both stationary and at one temperature before the start of the motion, then the larger the piston velocity after the impulsive start the larger the Mach number associated with the shock wave produced, and the greater the changes in density and temperature across the gas layer formed near the piston. When one employs the NS (continuum) point of view, then a discontinuity appears at the wall in both the temperature and the fluid velocity at time $t = 0^+$, and the corresponding heat flux and normal stress are infinite, and this occurs even for low values of the piston velocity. Clearly, the NS equations do not predict the correct physical process at very early time. This raises the interesting question, for this nonsteady problem, whether a numerical solution of the NS equations for large time would be independent of developments at early time.

Because Eq. (14) is an analytic result and does not depend explicitly on time, it can be used to qualify a numerical solution of the NS equations, because one would expect (14) to provide the correct NS prediction as a numerical solution is sequentially improved. The need for a reliable numerical check is the principal reason why the temperature ratio in (14) was not inverted, to correspond more directly to Patterson's expression. On using the variables defined by Eq. (14), the analytical relation plots as a straight line, which is shown as a heavy dashed line in Fig. 1 (note: $q/pc = 5\hat{q}/\sqrt{2\gamma}$). The four numerical solutions shown in the figure were carried out for the case of a monatomic gas and a piston Mach number of unity ($M_{shock} = 1.869$), using a second-order finite-volume scheme (first-order time) together with a range of cell sizes (see Ref. [4] for identification of the scheme used). Time appears as a parameter along each curve, with large time corresponding to small values of the abscissa. The physical scale is set by the values of the undisturbed density ρ_0, speed of sound c_0, coefficient of viscosity μ_0, and cell length Δx. These quantities can be used to either define a reference cell Reynolds number or a reference cell Knudsen number through the kinetic-theory, hard-sphere relation

$$\mu = \frac{5\pi}{32}\rho\bar{C}\lambda, \tag{15}$$

where $\bar{C} = \sqrt{8RT/\pi}$ is the mean thermal speed and λ is the mean free path length. Because we are interested in comparisons with DSMC, it is physically more meaningful to use a reference cell Knudsen number, $Kn_0 = \lambda_0/\Delta x$, with $\tilde{x} = x/\lambda_0$, $\tilde{t} = t\bar{C}_0/\lambda_0$, and

$$\Delta\tilde{t} = \Delta t\bar{C}_0/\Delta x Kn_0 = \sqrt{\frac{8}{\pi\gamma}}(CFL/Kn)_0, \tag{16}$$

as measures of the physical scale. In Fig. 1 the numerical solutions are shown for $Kn_0 = 2, 4, 8, 16$ and we see that the largest value is needed to get good agreement with (14). Because the gas density near the piston surface is nearly four times the undisturbed density (see Fig. 3), this translates into $Kn_{wall} \approx 4$ and therefore we must have $\Delta x < \lambda_{wall}/4$ to obtain a reliable NS solution at early time. The conditions near $t = 0^+$ necessitated the use of a very small $\Delta\tilde{t}$. This led to the use of values of CFL ranging from 0.15 to 0.0375 as the Knudsen number was increased. At this point we do not know whether the range of the independent variable displayed in Fig. 1 corresponds to conditions where the NS system predicts the correct physics, only that the values employed are required for a consistent numerical solution of the NS equations.

In turning to a DSMC simulation, it is clear that the same reference cell Knudsen number, $Kn_0 = 16$, should initially be used in making a comparison. Figure 2 shows such a comparison for two times: a time at which the shock wave and the thermal layer are both still forming, $\tilde{t} = 4.64$ (1,600 time steps NS, 400 DSMC); and the time at which they just begin to separate, $\tilde{t} = 11.6$ (4,000 time steps NS, 1,000 DSMC). Numerical instability with NS at early time necessitated a smaller time step (factor of 4) than that used with DSMC. The dimensionless time employed is based on the collision time in the reference state and so these times are truly short. At the early time the temperature profiles match somewhat poorly overall, while at the later time the thermal layers, alone, begin to match rather well. Because density is a less sensitive variable, the match at both times is surprisingly good, considering the extremely short time represented. Because the DSMC method is computationally intensive, it was necessary to increase the values of $\Delta\tilde{t}$ and Δx by a factor of 4, and decrease the value of Kn_0 by the same factor, to study still larger time.

Figure 3 makes the same comparison after the shock wave and the thermal layer have clearly separated, $\tilde{t} = 46.4$ (16,000 time steps NS; 1,000 DSMC), and it is seen that agreement is very good, except at the shock front itself, for which it is well known that NS gives a poor prediction for shock-wave profile.

The inherent statistical fluctuations which are characteristic of the DSMC method, especially for a nonsteady problem for which extended time averaging is not possible, do not allow for a detailed study of small differences represented by the temperature slip seen in Figs. 2 and 3. Nevertheless, in Fig. 4 we attempt to make a comparison of the time dependent temperature slip at the piston surface for the two methods. In this case, the DSMC results were time averaged over a small local interval about each plotted point to reduce statistical scatter. These simulations were carried out with a number density of approximately 8,000 particle per cell near the piston surface and roughly one million particles for the entire simulation. DSMC results were obtained for $Kn_0 = 4, 8, 16, 32$ by sequentially reducing the cell size by a factor of 2 while holding λ_0 fixed. These data include the runs shown in Figs. 2 and 3, and likewise, are for the same conditions. Because of the varying cell size, it would be necessary to extrapolate the data for each run to the position of the piston surface in order to produce a consistent display, but this approach amplifies statistical scatter and proves impractical for such a time-dependent simulation with DSMC. The alternative was to select the center position of the largest DSMC cell ($Kn_0 = 4$) as the reference and display the data for all runs for that position. This approach has the added feature that it provides a consistency check on the DSMC method itself. As seen in Fig. 4, the DSMC data overlap nicely, demonstrating that convergence has been obtained. Two curves are shown for the NS calculation: the dashed curve was obtained by extrapolating the data to the piston surface; and the solid curve represents the value at the center position of the largest cell used in the DSMC method ($Kn_0 = 4$). For the NS calculation, the cell size for $Kn_0 = 16$ was used. The separation between the two curves shows that the temperature gradient near the piston surface is very steep necessitating the use of a small cell size. In view of the different curves displayed, the solid curve for NS should be compared with the DSMC data, which appears to suggests that the boundary conditions (7)-(11) for NS over predict the temperature slip for these conditions. For large time the two should agree fully, but it did not appear feasible to extend the DSMC runs to verify this with the computer workstation employed in this part of the study. When considering the fact that the NS equations are not expected to represent the correct physics for large nonequilibrum (for example, $q/pc > 0.1$ for $\tilde{t} < 50$, see Figs. 1 and 4), the agreement seen in Figs. 2-4 is very encouraging, since it confirms the accepted view that slip conditions at a surface represent the principal corrections needed to be added to the NS system when dealing with a slightly rarefied flow.

If any discrepancy exists between the values of the split kinetic fluxes defined by Eqs. (1)-(6) and the corresponding values from DSMC simulations, then the differences should be seen at the piston surface where nonequilibrium is the greatest. Fig. 5 presents the corresponding comparisons for the mass and energy split fluxes, and shows that the agreement, for a monatomic gas, is extremely good. In the DSMC simulations the positive split fluxes were obtained by monitoring the passage of individual particles as they left the gas and crossed the piston surface, while the negative split fluxes were obtained by monitoring the particle emission from the piston surface introduced by the DSMC boundary conditions. For the NS solution, the state of the flow from the numerical solution was used to evaluate the positive split fluxes using the defining equations (1)-(6). Similarly, the conditions representing the isothermal piston were used to compute the negative split fluxes.

In the case of a polyatomic gas, the Eucken approximation was introduced in [4] to develop the split fluxes for energy; and it is of interest to determine whether the particular approximation used is supported by DSMC. The same simulations were repeated for the case of an ideal diatomic gas, assuming rotational degrees of freedom are in equilibrium with translation ($\gamma = 7/5$), and a comparison of split fluxes for momentum and energy is shown in Fig. 6. The excellent agreement seen confirms that the Eucken approximation, as implemented in [4], is capturing the proper physics in the splitting of energy flux, for both the translational and rotational components.

IV. IMPULSIVELY STARTED FLAT PLATE

Viscous stress becomes the dominant nonequilibrium effect for an impulsively started flat plate, which provides an alternate environment for comparison. For the one-dimensional geometry of an infinite, impulsively started flat isothermal plate moving parallel to its surface in, say, the t_1 direction, the t_1 and t_2 coordinates may be disregarded in (1)-(6); and the shearing stress $\hat{\tau}_{nt1}^{CE}$, along with the normal heat-flux component $\hat{q}_n^{CE}$, become the principal nonequilibrium quantities. Again, for calculational purposes it is easier to consider a moving gas and a stationary plate. At the plate surface we may then set $S_n = 0$ and thus $\alpha_1 = 0$ and $\alpha_2 = 1/\sqrt{\pi}$. On using Eq. (1) to represent the gas near the plate and on using boundary condition (7), exactly the same density and temperature relations are found as for the impulsively started piston, given by (11).

On using (1) and (3) to represent the gas near a stationary surface, in which we set $\hat{q}_{t1}^{CE}$ to zero because of uniformity, and on using boundary condition (9), we find

$$(F_{t1-mom})_{surface} = \left[\frac{1}{\sqrt{\pi}} p S_{t1}\left(1 - \frac{1}{2}\tilde{\tau}_{nn}^{CE}\right) - \frac{1}{2} p \hat{\tau}_{nt1}^{CE}\right]_g . \tag{17}$$

The definition for the total flux of transverse momentum leads to the substitution $(F_{t1-mom})_{surface} = -\tau_{nt1}$, because $S_n = 0$. On solving for S_{t1}, we then obtain the relation

$$S_{t1} = -\frac{\sqrt{\pi}}{2}\left(1 - \frac{1}{2}\tilde{\tau}_{nn}^{CE}\right)^{-1} \hat{\tau}_{nt1}^{CE} . \tag{18}$$

The quantity S_{t1} represents the dimensionless velocity of the fluid next to a stationary surface, i.e., velocity slip. Although Eq. (18) does not depend directly on the value of the ratio of specific heats γ, if the velocity slip is based on the reference plate speed u_{plate}, and a plate Mach number M_{plate} is introduced, then the factor $\sqrt{\pi}/2$ is replaced by $\sqrt{\pi/2\gamma}/M_{plate}$ and the γ dependence becomes evident. Here again, if we neglect $\tilde{\tau}_{nn}^{CE}$ then the above relation can be shown to agree fully with Patterson's result [9] for velocity slip (cf. equation (31), p. 125). If boundary condition (10) is handled in the same way as for the piston, and if the quadratic terms $S_{t1}\hat{\tau}_{nt1}$ and S_{t1}^2 are dropped, then exactly the same relation for the temperature slip as for the impulsively started piston is gotten, i.e., Eq. (14).

Just as for the case of the impulsively started piston, Eq. (18) can be used to qualify a numerical solution of the NS equations for an impulsively started flat plate. Except for a greater sensitivity to the impulsive start, which requires the use of still smaller time steps as the reference cell Knudsen number is increased, the conclusions drawn are essentially the same as those found in the study that led to the data presented in Fig. 1, and will not be repeated. Likewise, in order to emphasize nonequilibrium effects, an isothermal plate and a Mach number of unity were selected as appropriate conditions for study.

Using the more descriptive frame of reference where the gas is initially stationary and the plate is given an impulsive start, NS and DSMC results for velocity are displayed and compared in Fig. 7, at the dimensionless times $\tilde{t} = 12.4$ and $\tilde{t} = 68.0$. As can be seen, even though the velocity slip is fairly large at these short times, the NS solution compares extremely well with the DSMC results. In Fig. 8 the gas velocity at the surface of the plate is displayed as a function of time, showing that it approaches the plate velocity asymptotically. The DSMC results were obtained for $Kn_0 = 4$ and 8; and data for both runs were plotted for the location corresponding to the center position of the largest cell, $Kn_0 = 4$. The complete overlap of the symbols clearly demonstrates consistency, or convergence, in the DSMC results. In the case of the NS solution, the data for $Kn_0 = 12$ were used and extrapolated to the plate surface (dashed curve); the data were also evaluated at the center position of the largest cell (solid curve) used in the DSMC simulations. As the gradient near the plate is more modest here, the agreement is sufficiently close that one does not have to distinguish between the different curves. Equation (18) shows that the magnitude of $\hat{\tau}_{nt1}^{CE}$ is virtually the same as the slip $(1 - u/u_{plate})$ seen in the figure. Therefore, the degree of nonequilibirum is quite large, yet the NS prediction for velocity slip agrees very nicely with DSMC for these rather extreme conditions.

Continuing with comparisons for the split kinetic fluxes evaluated at the plate surface, Fig. 9 presents the results for the case of a monatomic gas, and the agreement seen is remarkably good. Likewise, Fig. 10 presents the split fluxes for a diatomic gas, showing equally good agreement. These quantities are displayed for a frame of reference where the gas is initially stationary and the plate is given an impulsive start. Therefore, asymptotic results deduced from Eq. (1)-(6) must be transformed to obtain the limiting values seen in Figs. 9 and 10. Beyond the excellent comparisons seen; the most important observation relates to the component quantities making up the energy split fluxes for the diatomic gas. It is clear that the translational and rotational degrees of freedom are being properly handled, and therefore, the approach used in Ref. [4], in introducing the Eucken approximation, appears to be working well.

V. LID-DRIVEN CAVITY FLOW

In the two cases studied above, heat flux and viscous stress were separately dominant; but both can become important in the lid-driven cavity problem, and an element of complexity is added by the two dimensions of the flow. However, focus will be placed on the steady-state condition for which the CFL restriction should not be as severe as for the case of an impulsive start. Here again, it is useful to assume isothermal surfaces to produce a large degree of nonequilibrium. On the other hand, the lid Mach number was set to $M_{lid} = 0.5$ so that nonequilibrium effects in the corners for steady state would not be unduly large. The reference Knudsen number, based on the dimension of the square cavity L, and defined by $Kn_L = \lambda_0/L$, was set equal to 0.01, where λ_0 is the mean free path length evaluated at the wall temperature and the initial state of the gas. The value of the Knudsen number was chosen so as to correspond to the near-continuum regime where NS is expected to be valid and the DSMC simulation does not become overly intensive. In the following, discussion will be limited to the case of a diatomic gas, as the monatomic case has been adequately covered above.

A steady state, two-dimensional NS solution, based on a 128×128 square mesh, is presented in Fig. 11 showing the component of velocity lying parallel to the lid. In the figure, the lid is on the near face and moves from left to right, for which the velocity is defined to be negative. The effect of velocity slip is clearly seen, both on the lid itself and at the two corners formed by the lid and walls. No slip would correspond to the magnitude of the dimensionless fluid velocity u/c_0 being equal to the lid Mach number, in this case 0.5. The view shown is useful in serving as a mental aid in presenting the comparisons to be reviewed below. For example, in the views that follow, the lid together with the two faces on either side will be unwrapped and displayed in planar form when various boundary quantities are compared.

In order to judge the validity of the numerical solution presented in Fig. 11, analytical relations similar to Eqs. (14) and (18) are needed. Using a coordinate system where n is taken to be perpendicular to the lid, $t1$ is parallel to the lid and $t2$ ignorable, then at various points along the lid one would expect the stresses τ_{nt1}^{CE} and τ_{nn}^{CE} and the heat flux components q_n^{CE} and q_{t1}^{CE} to be important. On this basis the slip relations found above may have to be generalized. When the algebra leading to (11) is repeated using $S_n = 0$ alone, exactly the same relations are found. A slight generalization to (18) is required, given by

$$S_{t1} = -\left(1 - \frac{1}{2}\hat{\tau}_{nn}^{CE}\right)^{-1}\left[\frac{\sqrt{\pi}}{2}\hat{\tau}_{nt1}^{CE} + \frac{1}{2}\hat{q}_{t1}^{CE}\right], \tag{19}$$

which introduces the heat flux component aligned with the lid, a quantity that may be important in the corners. More terms must be retained in the generalization of (13), for the temperature slip, which becomes

$$\left(1 - \frac{1}{2}\hat{\tau}_{nn}^{CE}\right)\frac{T_w}{T_g} = 1 - \left(\frac{\gamma-1}{\gamma+1}\right)\left[5\sqrt{\pi}\hat{q}_n^{CE} + \left(\frac{3\gamma-1}{2(\gamma-1)} + S_{t1}^2\right)\hat{\tau}_{nn}^{CE}\right] + 2\left(\frac{\gamma-1}{\gamma+1}\right)S_{t1}\left[S_{t1} + \sqrt{\pi}\hat{\tau}_{nt1}^{CE} + \hat{q}_{t1}^{CE}\right]. \tag{20}$$

In developing Eq. (20), the coordinate system in which the gas is moving and the wall is stationary was again used. Therefore, a transformation must be introduced when (20) is used to analyze the moving lid. Because of the complexity of (19) and (20), the approach employed in Fig. 1 is less useful here. Here too, Eqs. (19) and (20) can be shown to reduce to Patterson's results [9].

In the coordinate system defined by Fig. 11, the velocity component u lies parallel to the lid while the velocity component v lies parallel to the two faces on either side of the lid. Therefore, if we unwrap the adjacent faces and display the tangential velocity along the surface as a function of the surface position for the NS solution, we obtain the function seen in the top view of Fig. 12, shown as a solid curve. This function contains both u and v and is not merely a copy of the edge values for u shown in Fig. 11. The corresponding theoretical prediction is given by Eq. (19) and is shown as the heavy dotted curve (a transformation must be applied to (19) to obtain the values along the lid). It is clear that agreement is only found outside the two corner regions. This can be understood by reviewing the plot shown in the bottom view of the figure, which gives the normal velocity component S_n as a function of s. Equation (19) was derived on the basis of the assumption $S_n = 0$ and it is clear from the plot for S_n that the assumption does not hold in the two corners. Therefore, use of Eq. (19) as a check on the validity of the numerical solution obtained must be confined to areas near $s = 0.5, 1.5, 2.5$; and this check clearly shows that reliable numerical results were in fact obtained.

Practical considerations made it necessary to limit the DSMC simulation to a 64×64 array of cells. Past experience with the DSMC method for a steady state problem led to the decision to use an average number density of approximately 64 particles per cell, leading to a total of roughly 0.25×10^6 particles employed in the simulation. Roughly 12,000 time steps were used in the time averaging of the data which gave a sample size for each cell of approximately 0.75×10^6. In this case it was more appropriate to run the simulation on a parallel supercomputer, which required a total of 116 node-hours to carry out the comparisons. The top view of Fig. 13 compares the NS solution against DSMC results for the tangential velocity versus the surface position. In each case the data were projected to the position of the surface for comparison. As can be seen, the correspondence is quite complete, even including sharp spikes in the two corners. Consequently, the NS prediction for the slip velocity is quite outstanding for these conditions. Because of the low Mach number chosen, $M_{lid} = 0.5$, the temperature rise is fairly small (less than 5%) and the DSMC data for temperature exhibit considerable statistical scatter, as is seen in the bottom view in the figure, and a fully equivalent judgment concerning the NS temperature slip, DSMC results, and Eq. (20) cannot be made.

Because the wall temperature is specified for an isothermal wall, the NS solution only controls the density of the hypothetical wall gas ρ_w (see Eq. (11)). Furthermore, because the emission from the wall is controlled by a Maxwellian distribution in the particular application (isothermal wall) of the KFVS method being considered, the split fluxes directed out of the wall are not overly sensitive to the NS solution. Thus, it makes sense to focus attention on the

split fluxes directed out of the gas and into the wall. Figure 14 gives a comparison for this single component of the two kinetic split fluxes for energy, where the upper set is for the translational energy component and the lower set is for the rotational energy component. As seen, the NS predictions compare extremely well with the DSMC results, including the excursions in the two corners. Likewise, the good match for rotational energy shows that the form of the Eucken approximation employed in the development of the KFVS method proves to be valid even for these conditions.

Although prediction of the values of the fluid variables at the lid and walls represents a more severe test of the KFVS theory than that for the interior regions of the lid-driven cavity problem, it is also of interest to consider one comparison for the entire flow. Figure 15 displays the v-component of velocity for a number of transverse slices positioned along the x axis. The NS solution is given by the solid curves and the DSMC results by the symbols, likewise showing good agreement between the two.

VI. CONCLUDING REMARKS

The method of kinetic flux-vector splitting for the Navier-Stokes equations was introduced primarily as the continuum counterpart to the DSMC method in the eventual development of a hybrid scheme [4]. A principal requirement in joining the two methods at a fluid interface is the presence of compatible split fluxes. Because NS is not valid in rarefied flow and the use of the DSMC method becomes overly costly in the deep continuum, matching must be carried out in the near-continuum where the flow is only slightly rarefied, a degree of rarefaction which may be defined as the regime where the local cell Knudsen number is of order unity. These conditions were considered in selecting the test conditions reported above and very good agreement was found for the split fluxes in the two schemes, even for the extreme nonequilibrium conditions found near isothermal surfaces, conditions surely more severe than those found at most any other interface located within the flow. Because the split fluxes for mass and momentum do not depend on γ, it is certainly expected that one would obtain equally good results for monatomic and diatomic gasses for these quantities. However, the split fluxes for energy clearly depend on the additional internal energy carried by polyatomic molecules, and for this case it was necessary to make use of a particular interpretation of the Eucken model to carry out the splitting (see Ref. [4]). Therefore, comparisons such as those seen in Figs. 10 and 14 prove to be of great value in justifying the assumptions made. Beyond the fact that the split fluxes defined in KFVS and DSMC have been shown to agree remarkable well, which is an important step in the development of a hybrid scheme, it was also shown that the slip conditions for temperature and velocity at a material surface also agreed quite well. This is also a significant result because the flow is fully expected to be slightly rarefied near a material surface for most conditions for which a hybrid scheme would be employed.

VII. ACKNOWLEDGMENTS

This work was supported in part by NASA Grant NCC2-5072. Access to the CACR parallel supercomputer operated by Caltech, on behalf of the Center for Advanced Computing Research, was provided by the Numerical Aerosciences Simulation program at NASA-Ames Research Center.

---

[1] D. Baganoff and J. McDonald, *Phys. Fluids A* **2** (7), 1248 (1990).
[2] G. A. Bird, *Annu. Rev. Fluid Mech.* **10**, 11 (1978).
[3] G. A. Bird, *Molecular Gas Dynamics and the Direct Simulation of Gas Flows* (Clarendon Press, Oxford, 1994).
[4] S. Y. Chou and D. Baganoff, *J. Comput. Phys.* to be published.
[5] T. Denery, Ph. D. thesis, Stanford University, 1995.
[6] S. M. Deshpande, AIAA Paper 86-0275 (1986).
[7] J. C. Mandal and S. M. Deshpande, *Comput. & Fluids* **23**, 447 (1994).
[8] J. McDonald, Ph. D. thesis, Stanford University, 1990.
[9] G. N. Patterson, *Molecular Flow of Gases* (John Wiley, New York, 1956).
[10] V. P. Shidlovskiy, *Introduction to the Dynamics of Rarefied Gases* (American Elsevier, New York, 1967).

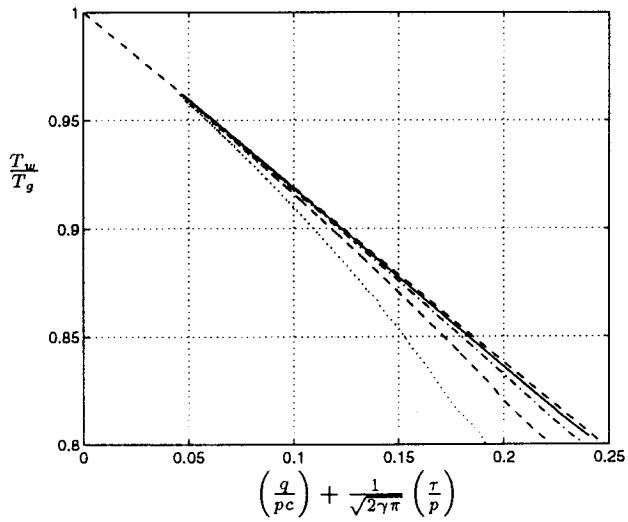

FIG. 1. Gas temperature at the surface of an impulsively started isothermal piston moving into a stationary monatomic gas. Theoretical relation given by Eq. (14), - - - - . Numerical integration of the NS equations for $M_{piston} = 1$, $\gamma = 5/3$, and reference cell Knudsen number $Kn_0 = 2$, ... ; 4, - - - - ; 8, - . - . - ; and 16, —— .

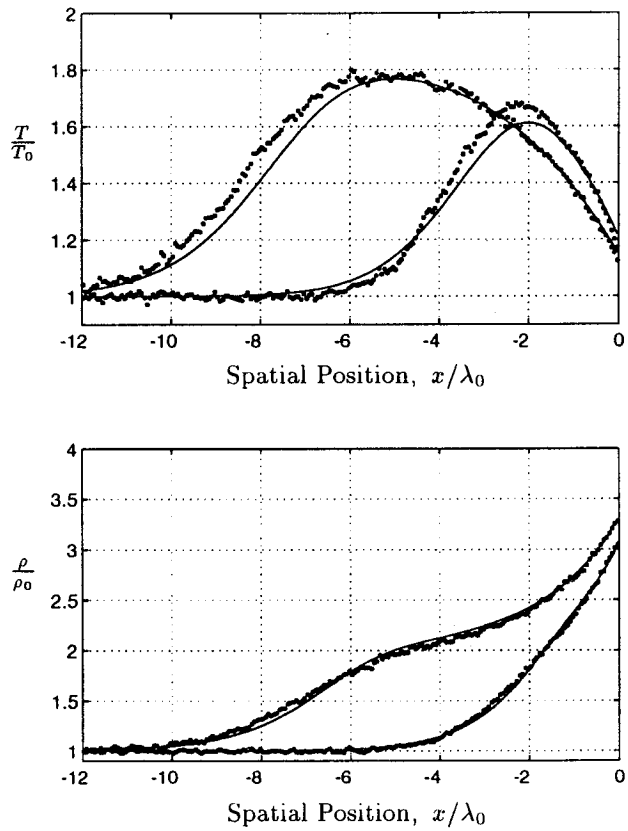

FIG. 2. Gas temperature and density ahead of an isothermal piston (located at $\tilde{x} = 0$) for NS (solid curves) and DSMC (symbols), at two early times in the formation of the shock wave and the thermal layer, for $M_{piston} = 1$ and $\gamma = 5/3$. Dimensionless times correspond to $\tilde{t} = 4.64$ and $\tilde{t} = 11.6$.

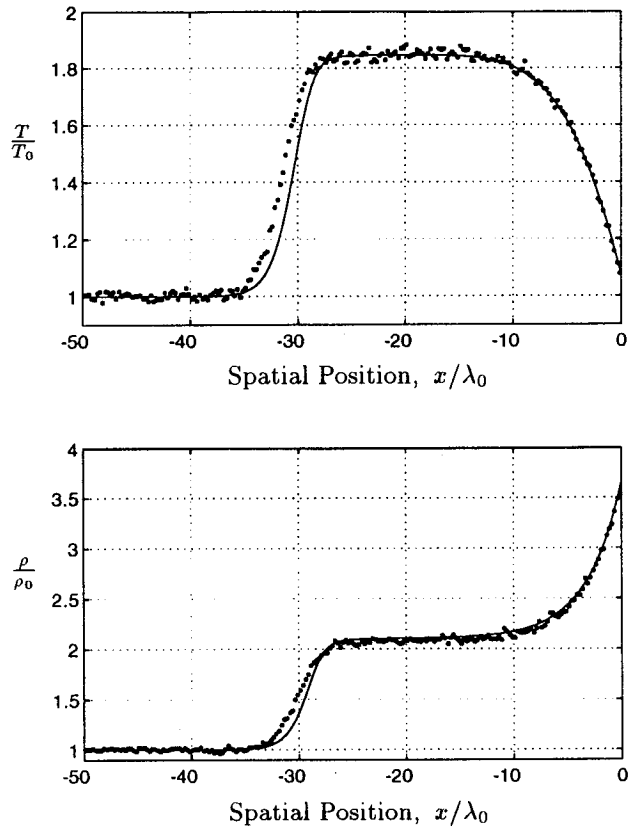

FIG. 3. Gas temperature and density ahead of an isothermal piston (located at $\tilde{x} = 0$) for NS (solid curves) and DSMC (symbols), for $M_{piston} = 1$, $\gamma = 5/3$, and at a time $\tilde{t} = 46.4$ when the shock wave and thermal layer have clearly separated, showing a well defined thermal layer. The DSMC results are for $Kn_0 = 4$ while the NS results are for $Kn_0 = 16$, i.e., Δx for NS is 4 times smaller than for DSMC.

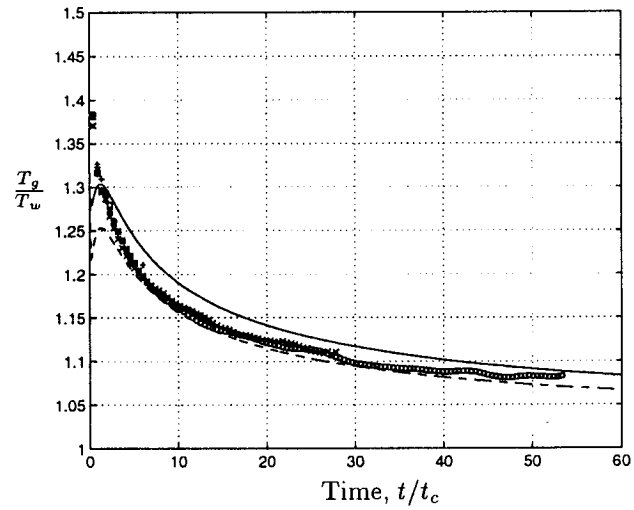

FIG. 4. Gas temperature at the surface of an isothermal piston versus dimensionless time, for $M_{piston} = 1$ and $\gamma = 5/3$. DSMC cell dimensions correspond to $Kn_0 = 2$, o; 4, x; 8, $*$; 16, $+$. The NS solution was evaluated for $Kn_0 = 16$ and projected to the piston surface (dashed curve); same solution was evaluated at cell center for the largest DSMC cell (solid curve).

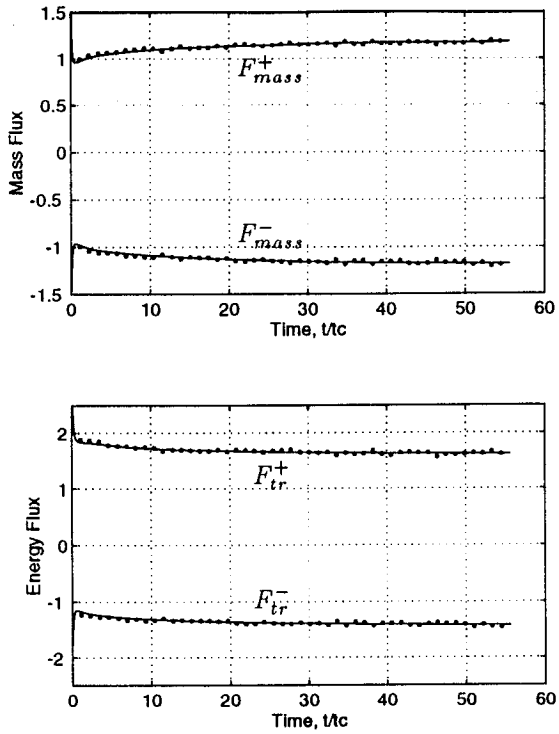

FIG. 5. Kinetic split fluxes evaluated at the surface of an isothermal piston, for $M_{piston} = 1$ and $\gamma = 5/3$. The numerical solution of the NS equations (solid curves) are compared with results from a DSMC simulation (symbols). Mass and energy split fluxes are referenced to the values $\rho_0 c_0$ and $\rho_0 c_0^3$, respectively.

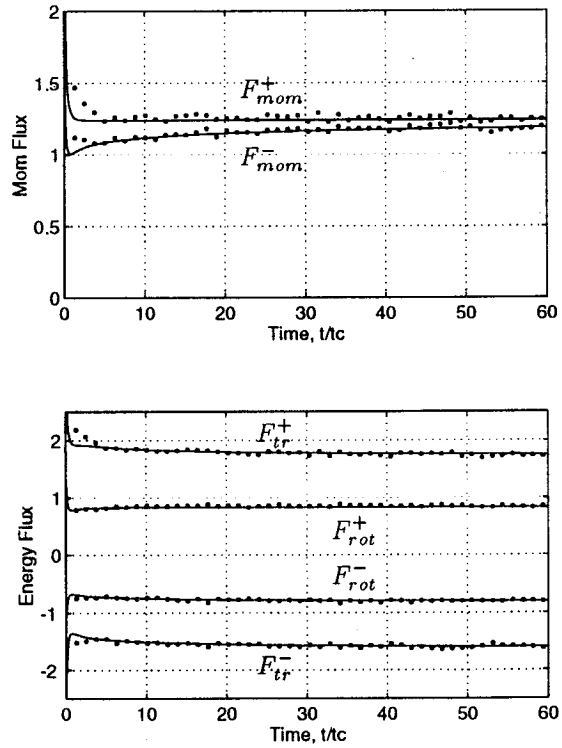

FIG. 6. Kinetic split fluxes evaluated at the surface of an isothermal piston, for $M_{piston} = 1$ and $\gamma = 7/5$. Momentum and energy split fluxes are referenced to the values $\rho_0 c_0^2$ and $\rho_0 c_0^3$, respectively.

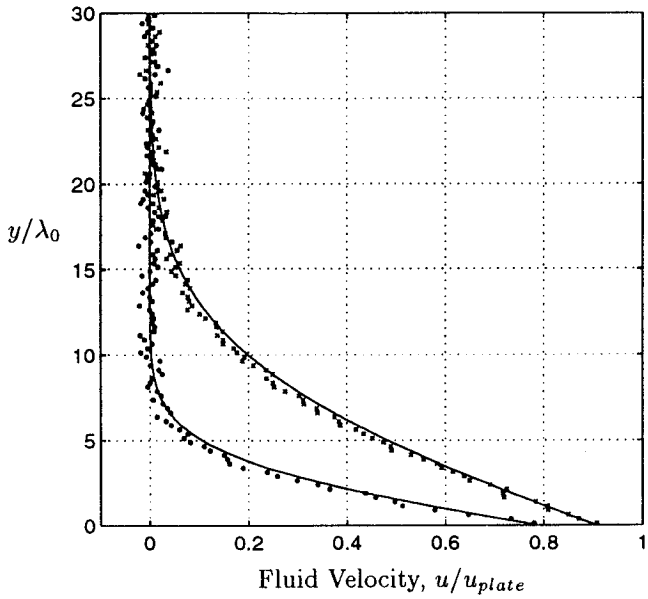

FIG. 7. Velocity distribution above an impulsively started isothermal flat plate, for $M_{plate} = 1$ and $\gamma = 5/3$. The two times shown are for $\tilde{t} = 12.4$ and 68.0, with NS solution (solid curves) and DSMC simulation (symbols).

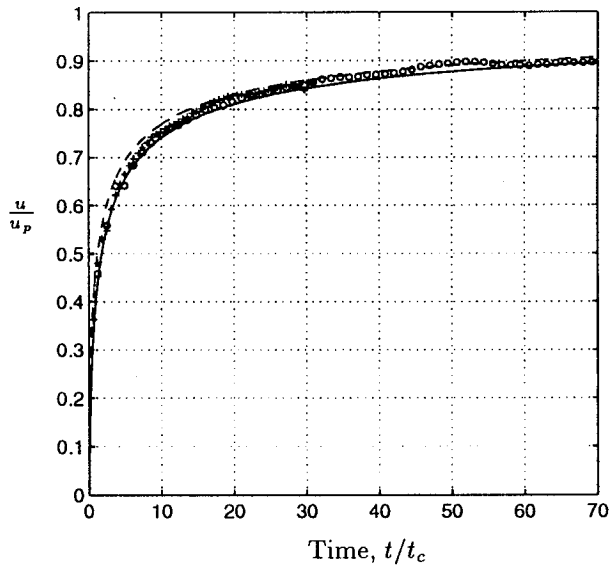

FIG. 8. Gas velocity at the surface of an impulsively started isothermal flat plate versus time, for $M_{plate} = 1$ and $\gamma = 5/3$. NS solution for $Kn_0 = 12$, with extrapolation to surface (dashed curve) and location at cell center for largest DSMC cell (solid curve). DSMC simulation for $Kn_0 = 4$, o; 8, $+$.

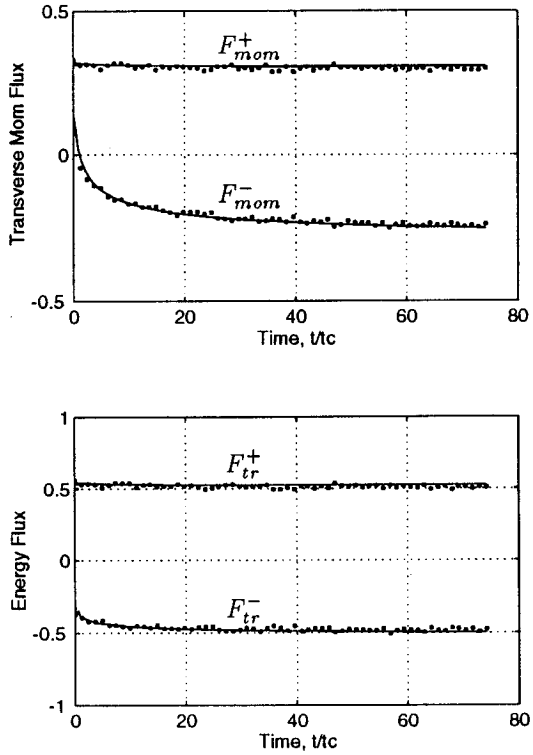

FIG. 9. Kinetic split fluxes evaluated at the surface of an isothermal flat plate, for $M_{plate} = 1$ and $\gamma = 5/3$. The numerical solution of the NS equations (solid curves) are compared with results from a DSMC simulation (symbols). Momentum and energy split fluxes are referenced to the values $\rho_0 c_0^2$ and $\rho_0 c_0^3$, respectively.

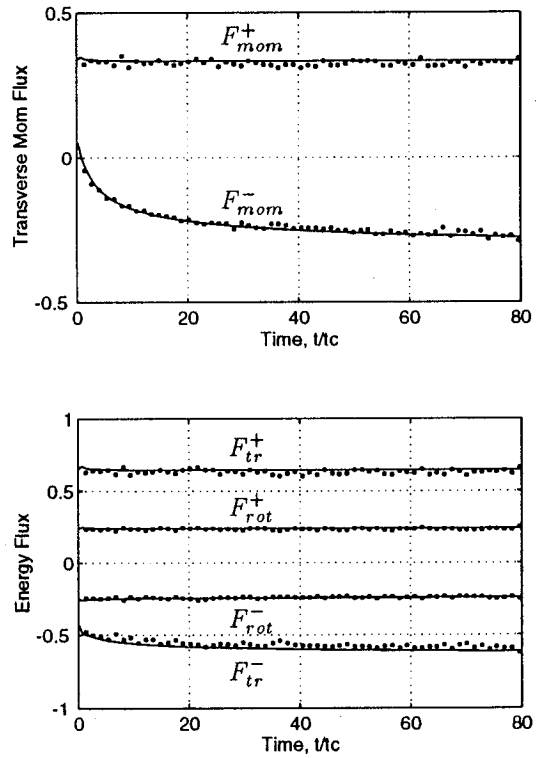

FIG. 10. Kinetic split fluxes evaluated at the surface of an isothermal flat plate, for $M_{plate} = 1$ and $\gamma = 7/5$. The numerical solution of the NS equations (solid curves) are compared with results from a DSMC simulation (symbols). Momentum and energy split fluxes are referenced to the values $\rho_0 c_0^2$ and $\rho_0 c_0^3$, respectively.

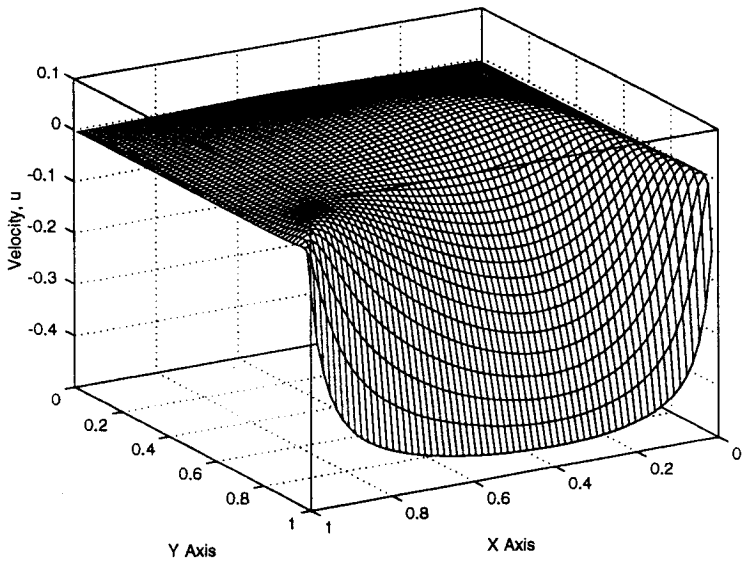

FIG. 11. Variation of the u-component of velocity for the NS solution to the lid-driven cavity problem. Lid velocity is from left to right on the near face, with $M_{lid} = 0.5$ and $\gamma = 7/5$.

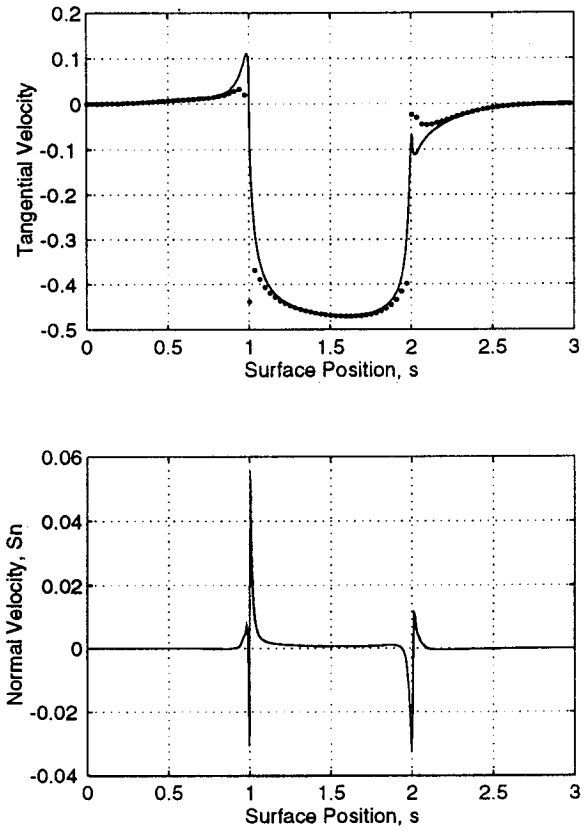

FIG. 12. Tangential and normal velocities at the surface of the lid and cavity for the NS solution. Upper view: numerical solution of the NS equations (solid curve) and the theoretical expression, Eq. (19), for the tangential velocity u_t/c_0 (dotted curve). Lower view: velocity component normal to the surface of the cavity, S_n, for the NS solution.

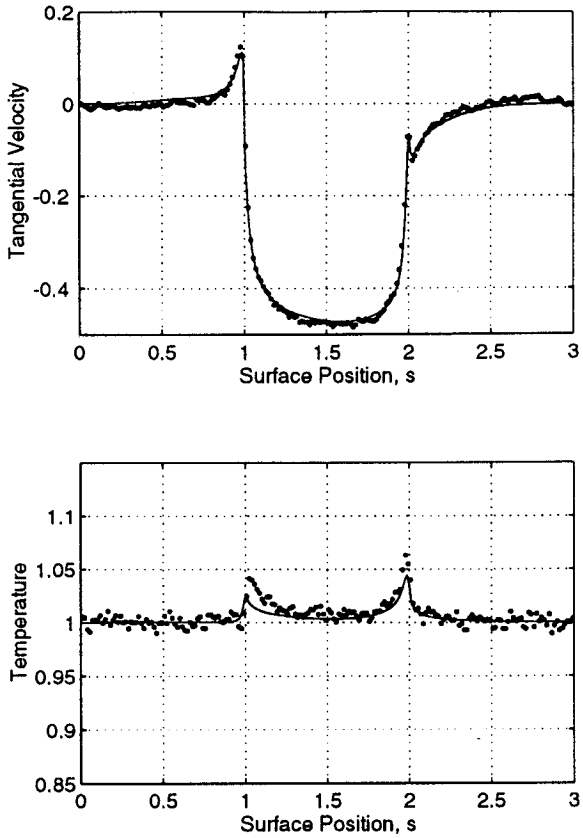

FIG. 13. Tangential velocity, u_t/c_0, and temperature,T/T_0, at the surface of the lid and cavity for the NS solution (solid curves) versus result for a DSMC simulation (symbols).

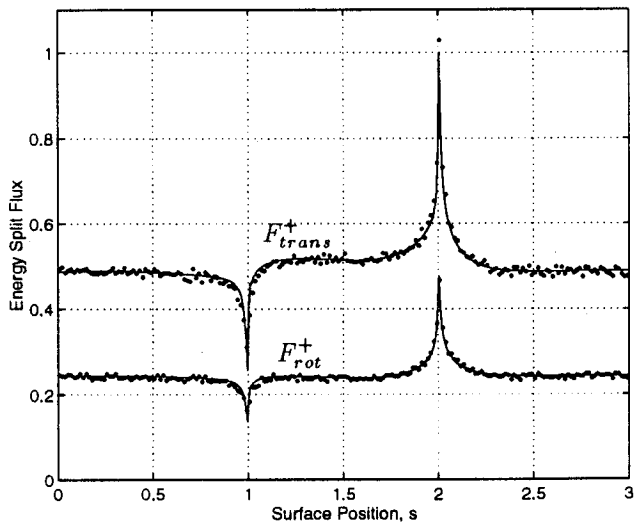

FIG. 14. Translational (upper curves) and rotational (lower curves) energy split fluxes at the surface of the lid and cavity for NS (solid curves) and DSMC (symbols). Energy split fluxes are referenced to the value $\rho_0 c_0^3$.

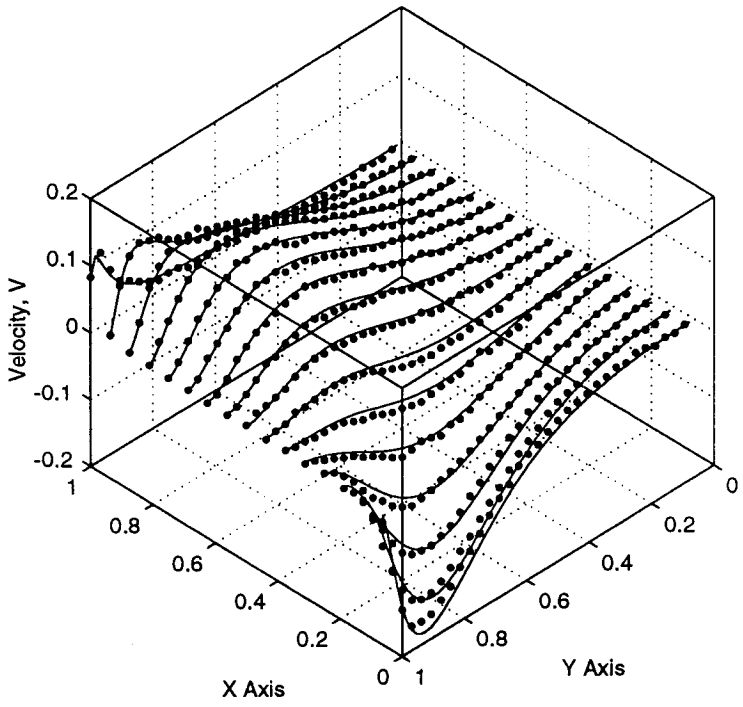

FIG. 15. Comparison of the v-component of velocity, v/c_0, in the cavity for NS (solid curves) and DSMC (symbols).